



저작자표시-비영리-변경금지 2.0 대한민국

이용자는 아래의 조건을 따르는 경우에 한하여 자유롭게

- 이 저작물을 복제, 배포, 전송, 전시, 공연 및 방송할 수 있습니다.

다음과 같은 조건을 따라야 합니다:



저작자표시. 귀하는 원저작자를 표시하여야 합니다.



비영리. 귀하는 이 저작물을 영리 목적으로 이용할 수 없습니다.



변경금지. 귀하는 이 저작물을 개작, 변형 또는 가공할 수 없습니다.

- 귀하는, 이 저작물의 재이용이나 배포의 경우, 이 저작물에 적용된 이용허락조건을 명확하게 나타내어야 합니다.
- 저작권자로부터 별도의 허가를 받으면 이러한 조건들은 적용되지 않습니다.

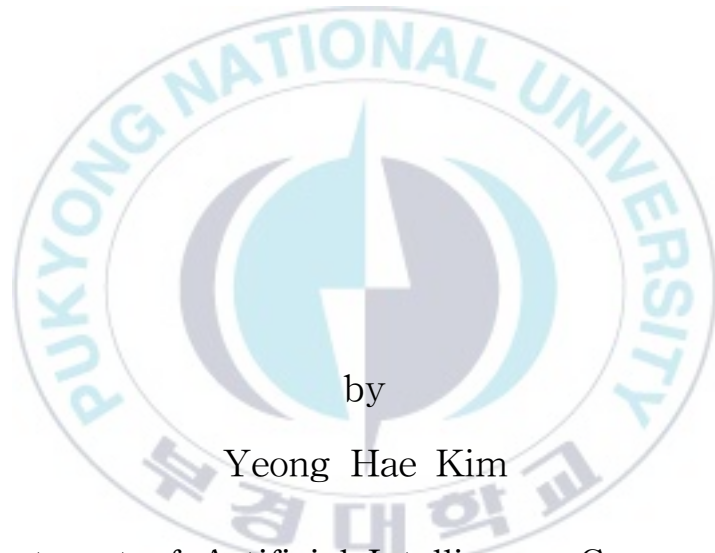
저작권법에 따른 이용자의 권리는 위의 내용에 의하여 영향을 받지 않습니다.

이것은 [이용허락규약\(Legal Code\)](#)을 이해하기 쉽게 요약한 것입니다.

[Disclaimer](#)

Thesis for the Degree of Master of Engineering

Optical Wireless based Unmanned Vehicle Communication



by

Yeong Hae Kim

Department of Artificial Intelligence Convergence

The Graduate School

Pukyong National University

February 2023

Optical Wireless based Unmanned Vehicle Communication

광무선 기반의 무인 이동체 통신

Advisor. Prof. Yeon Ho Chung

by
Yeong Hae Kim

A thesis submitted in partial fulfillment of the requirements for
the degree of

Master of Engineering

in Department of Artificial Intelligence Convergence, The
Graduate School, Pukyong National University

February 2023

Optical Wireless based Unmanned Vehicle Communication

A dissertation

by

Yeong Hae Kim

Approved by:

Professor Kyu Chil Park,
(Chairman)

Professor Sang Seok Yun,
(Member)

Professor Yeon Ho Chung,
(Member)

February 17, 2023

Table of contents

List of Figures	iv
List of Tables	vi
Abstract	vii
1. Introduction	1
1.1 Optical Wireless Communications	1
1.1.1 OWC assisted Unmanned Vehicle	2
1.2 Research Motivations	4
1.3 Thesis Objective	5
1.4 Chapter Organization	6
2. Optical Array Selection Transmit Diversity Scheme · 7	7
2.1 UAV-assisted OWC	7
2.2 Maximal Selection Transmit Diversity	8
2.3 System Model	8
2.3.1. CDF of the largest Order Statistics	11
2.3.2. Average Bit Error Rate	12
2.4 Results and Analysis	12
3. Switch-and-Stay Combining over Correlated Channels	16
3.1 FSK-SIM with Correlated Branches	16
3.2 System Model	16
3.3 Performance Analysis	18
3.3.1. Average BER when $\chi \leq \chi_{Th}$	20

3.3.2. Average BER when $\chi > \chi_{Th}$	21
3.4 Results and Discussion	22
4. Impact of Hovering on Laguerre-Gaussian Beam Propagation	25
4.1 Hovering Impact on UAV-to-Ground Links	25
4.2 Laguerre-Gaussian Beam Propagation	25
4.3 System Model	25
4.3.1. Hovering Loss	26
4.4 Results and Discussion	28
5. Link Connectivity in UAV Optical Ad-Hoc Network	31
5.1 UAV-to-UAV Communication	31
5.2 Connectivity in One-dimensional UAV Ad-hoc Network	32
5.3 Results and Discussion	34
6. Energy Harvesting Scheme for Simultaneous Lightwave Information and Power Transfer	37
6.1 Underwater Optical Wireless Communication	37
6.2 Simultaneous Lightwave Information and Power Transfer	37
6.3 Optimal Energy Harvesting	38
6.3.1. Multi-layer turbulence channel	42
6.4. Problem Formulation	44
6.4.1. Optimization problem with deterministic energy harvesting rate	44
6.4.2. Optimization problem with nondeterministic energy harvesting	44

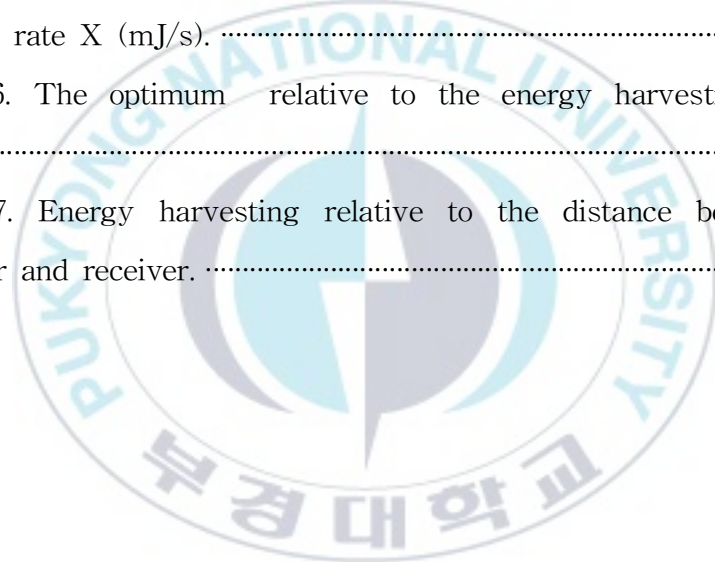
rate	46
6.5 Results and Discussion	48
7. Conclusion	54
References	57
List of Publications	62
Journal Papers	62
Conference Papers	63



List of Figures

Figure 1.1. Classification of the OWC systems.	2
Figure 2.1. Link geometry of ground-to-UAV optical communication. ...	9
Figure 2.2. BER relative to the average received SNR for different turbulence strength.	14
Figure 2.3. BER relative to the link range for different turbulence strength.	15
Figure 3.1. Switch-and-stay combining equipped with subcarrier frequency-shift keying for ground-to-UAV optical link.	18
Figure 3.2. Average BER performance relative to the average received SNR for different threshold and link range values.	23
Figure 3.3. Impact of correlation on sub-carrier intensity modulated frequency shift keying equipped with switch-and-stay combining diversity technique.	24
Figure 4.1. UAV-to-ground optical communication link geometry.	26
Figure 4.2. Transmitted beam	29
Figure 4.3. Intensity loss due to hovering relative to the propagation distance.	29
Figure 5.1. One-dimensional UAV optical ad-hoc network.	32
Figure. 5.2. Impact of the threshold distance on the probability of connectivity.	35
Figure. 5.3. Probability of connectivity relative to the UAV density for different neighbors.	36

Figure 5.4. Probability of connectivity against the neighboring UAVs.	36
Figure 6.1. A schematic diagram showing the simultaneous information and power transfer.	39
Figure 6.2 Receiver section.	40
Figure 6.3. Throughput (bits/s/Hz) relative to the time allocated to the energy harvesting (t_e).	50
Figure 6.4. Throughput (bits/s/Hz) relative to the received SNR (dB).	50
Figure 6.5. Throughput (bits/s/Hz) as a function of t_e and the energy harvesting rate X (mJ/s).	51
Figure 6.6. The optimum t_e relative to the energy harvesting rate X (mJ/s).	51
Figure 6.7. Energy harvesting relative to the distance between the transmitter and receiver.	52



List of Tables

Table 2.1. Simulation parameters [16].	13
Table 4.1. Simulation parameters.	28
Table 6.1 Simulation parameters for underwater optimal value.	49

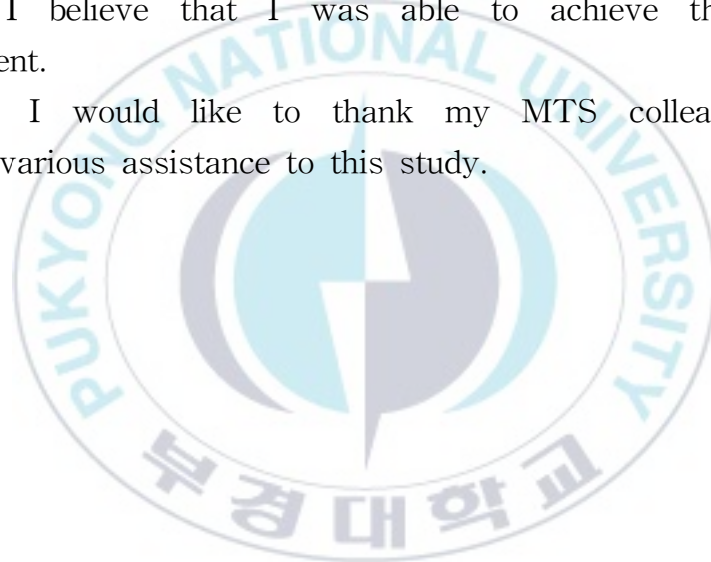


Acknowledgement

I would like to present my gratitude primarily to my supervisor, Professor Yeon Ho Chung not only for his guidance and unconditional support but also for providing me with the opportunity to pursue the master degree in the Mobile Transmission Systems (MTS) at Pukyong National University.

I would like to express deep gratitude to my mentor, Sudhanshu Arya, in the MTS laboratory. Thanks to your sincere support, I believe that I was able to achieve the present achievement.

Finally, I would like to thank my MTS colleagues who provided various assistance to this study.



Optical Wireless based Unmanned Vehicle Communication

Yeong Hae Kim

Department of Artificial Intelligence Convergence, The Graduate School,
Pukyong National University

Abstract

Optical wireless communication (OWC) has emerged as a promising technology for high-speed, high-capacity communication in the next generation. OWC has many advantages over conventional RF communications, such as abundance of unregulated bandwidth, miniaturized transceivers using lower power and immunity to the electromagnetic interference from already heavily used RF equipments. OWC uses optical carrier, i.e., infrared (IR), visible light, ultraviolet (UV). In OWC, one of the characteristics is that the OWC using IR and visible light compose the line of sight (LOS) link. In other words, if a large obstacle is between the transmitter and the receiver, the communication link is disconnected. To overcome this challenge, unmanned aerial vehicle can be used to relay the signal. UAV can be composed in the network to support wireless communication infrastructure. An unmanned vehicle is also used underwater to compose the network. Autonomous underwater vehicles (AUV) support maritime applications and can communicate each other.

In the first three studies are explored to design and model various unmanned vehicle communication link. The first study proposes the maximal selection transmit diversity scheme for ground-to-UAV optical links and investigates communication performance. The second employs switch-and-stay combining over correlated channel and frequency shift keying sub-carrier intensity modulation for ground-to-UAV links and investigates communication performance. The third considers Laguerre-Gaussian beam for UAV-to-ground and investigates the impact of hovering.

In the fourth study, we estimate the link connectivity between the unmanned

vehicles. In one-dimension, the UAV position follows a Poisson point process.

The final study proposes an optimal and energy-efficient time-splitting based simultaneous light-wave information and power transfer (SLIPT) for underwater optical wireless communications. We consider a multi-layer turbulence-induced underwater optical channel with each layer experiencing independent and nonidentically distributed oceanic turbulence.



광무선 기반의 무인 이동체 통신

김영해

부경대학교 대학원 인공지능융합학과

요약

광무선통신(OWC)은 차세대 고속, 고용량 통신의 유망 기술로 떠오르고 있다. OWC는 규제되지 않은 대역폭의 풍부함, 저전력을 사용하는 소형화된 트랜시버, 이미 많이 사용되는 RF 장비의 전자기 간섭에 대한 내성 등 기존 RF 통신에 비해 많은 이점을 가지고 있다. OWC는 광학 캐리어, 즉 적외선(IR), 가시광선, 자외선(UV)을 사용한다. OWC의 특징 중 하나는 IR과 가시광선을 이용하는 OWC가 LOS(Line of Sight) 링크를 구성한다는 점이다. 즉, 송신기와 수신기 사이에 큰 장애물이 있으면 통신 링크가 끊어진다. 이 문제를 극복하기 위해 무인 항공기를 사용하여 신호를 중계할 수 있다. 무선 통신 인프라를 지원하기 위해 네트워크에 UAV를 구성할 수 있다. 무인 차량도 네트워크를 구성하기 위해 수중에서 사용된다. 자율 수중 차량(AUV)은 해상 애플리케이션을 지원하고 서로 통신할 수 있다.

처음 세 연구에서는 다양한 무인 차량 통신 링크를 설계하고 모델링하기 위한 탐구를 진행한다. 첫 번째 연구는 지상-무인기 광링크를 위한 최대 선택 전송 다이버시티 방식을 제안하고 통신 성능을 조사한다. 두 번째는 지상-UAV 링크에 대한 상관 채널 및 주파수 편이 변조 부반송파 강도 변조에 대한 전환 및 유지 결합을 사용하고 통신 성능을 조사한다. 세 번째는 UAV-to-ground에 대한 Laguerre-Gaussian 빔을 고려하고 호버링의 영향을 조사한다.

네 번째 연구에서는 무인 차량 간의 링크 연결성을 추정한다. 1차원에서 UAV 위치는 포아송 포인트 프로세스를 따른다고 가정한다.

최종 연구에서는 수중 광 무선 통신을 위한 최적의 에너지 효율적인 시분할 기반 SLIPT(Simultaneous Light-Wave Information and Power Transfer)를 제안한다. 우리는 각 층이 독립적이고 동일하지 않게 분포된 해양 난기류를 겪는 다층 난기류 유도 수중 광학 채널을 고려한다.

1. Introduction

1.1 Optical Wireless Communications

Emergence of new applications, such as artificial intelligence (AI), virtual reality (VR), three-dimensional (3D) media, and the Internet of Everything (IoE), has generated huge amounts of traffic [1]. As the traffic increases, the demand for high-speed, high-capacity, high-integrity wireless communication increases. However, for radio frequency (RF), it is challenging to satisfy increasing demands because of its limited electromagnetic spectrum due to congested spectrum. Therefore, spectrum expansion toward the optical spectrum needs to be considered.

Optical wireless communication (OWC) refers to the transmission of information in an unguided propagation channel. OWC uses Infrared (IR), visible light, ultraviolet (UV) as optical carriers. In OWC, the transmitter is a light-emitting diode (LED) which has wide beam divergence and short transmission range, and a Light Amplification by the Stimulated Emission of Radiation (LASER) which has narrow beam divergence and long transmission range, while the receiver is a photodiode or a photon multiplier tube (PMT). Compared to the RF communication system, optical wavelengths have some potential advantages such as abundance of unregulated bandwidth, high channel capacity, miniaturized transceiver circuits with low transmit power, and immunity to the electromagnetic interference with widely used RF equipments [2].

The OWC systems can be divided into three categories: indoor communication, outdoor communication, underwater communication, as illustrated in Figure 1.1. Indoor communication employs visible light and IR as a carrier and has various links because it can utilize reflection.

Outdoor communication is commonly known as free-space optical (FSO) communication and can be divided into terrestrial and space links [3]. Underwater communication suffers severe water absorption at optical frequencies but at the blue-green wavelengths of electromagnetic spectrum, the attenuation is relatively low. For this reason, underwater communication usually employs blue-green wavelengths [4].

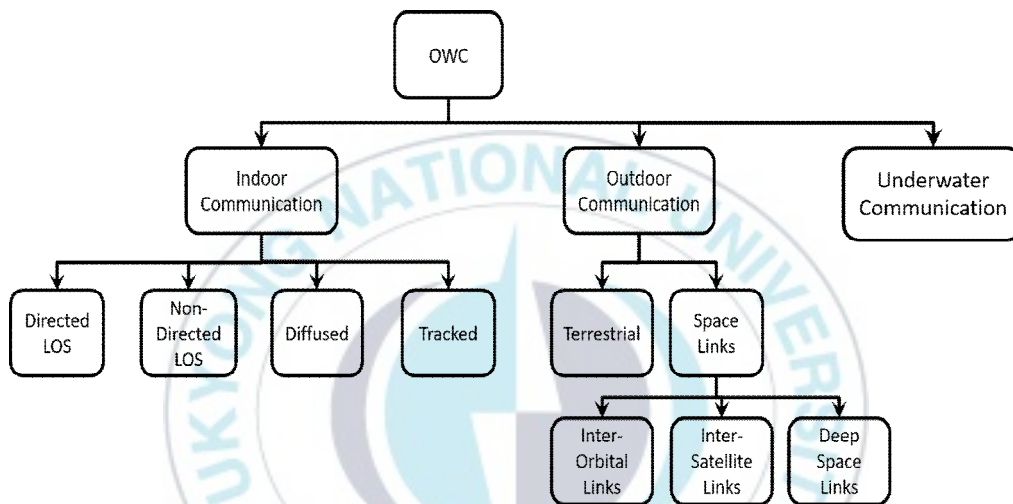


Figure 1.1. Classification of the OWC systems.

1.1.1 OWC assisted Unmanned Vehicle

In this thesis, we consider the two types of unmanned vehicle: unmanned aerial vehicle (UAV), autonomous underwater vehicle (AUV).

First, an UAV is referred to as a pilotless aircraft, a flying machine without an onboard human pilot or passengers. UAV can be used for various purposes by installing sensors or tools. For military use, reconnaissance and armed UAVs are mainly considered. Civilian applications include scientific research, search and rescue, traffic control tasks, and infrastructure support [5]. Because of the mobility of UAVs, UAV-assisted wireless or optical wireless communication can be a solution to several issues encountered in conventional wireless

communications. For example, signals can be relayed through UAVs when transceivers cannot see each other due to a large building, and UAVs can be quickly restored when a problem occurs in the communication infrastructure in a disaster situation [6].

An AUV is a robot that travels underwater without requiring input from an operator. For maritime applications such as underwater scientific data collection, environmental monitoring, harbor security and so on, underwater sensor network (USN) using AUV is required. However, there is a challenge with network lifetime which depends on battery capacity [7].



1.2 Research Motivations

6th-generation (6G) and beyond 5th-generation (B5G) will be developed and in use in the near future. As the new generation comes, new frequency bands such as millimeter-wave (mmWave) and optical spectra to overcome the issue of spectrum shortage and frequency congestion in RF are being considered. Furthermore, RF spectrum will not be sufficient to future wireless communications such as machine-type communications for autonomous systems and new devices using augmented reality and virtual reality [8]. However, optical spectra also have some challenges: turbulence-induced fading, blockage and so on [9]. We focus on the blockage problem which occurs when there are large obstacles enough to prevent a line of sight (LOS) link. The unmanned vehicle assisted communication can solve this problem by relaying the signal in the three dimensional space that can establish as LOS link. In the case of UAV, the mobility is useful for emergency network recovery and temporary communication link and mobility is also useful in compensating for communication quality degradation caused by environmental changes by moving their position [10].

1.3 Thesis Objective

With the above motivations, this thesis considers the following objectives:

- i. To design and model various unmanned vehicle communication links
- ii. To estimate the link connectivity between unmanned vehicles
- iii. To investigate an optimal technique for power problems in communication between AUVs



1.4 Chapter Organization

The remaining chapters in this thesis are outlined as follows. To design and model various unmanned vehicle communication links, an optical array selection transmit diversity scheme for ground-to-UAV optical links is studied in Chapter 2. For the same objective, a ground-to-UAV optical link with switch-and-stay combining over correlated channels is studied in Chapter 3. Impact of hovering on Laguerre-Gaussian beam propagation for UAV-to-ground optical communications is described in Chapter 4. To estimate the link connectivity between the unmanned vehicles, the link connectivity in one dimensional UAV optical ad-hoc network is studied in Chapter 5. To investigate the optimal techniques for power problems in communication between AUVs, an optimal energy harvesting scheme for simultaneous lightwave information and power transfer over multi-layer turbulence-induced underwater channel is studied in Chapter 6. Finally, conclusions are described in Chapter 7.

2. Optical Array Selection Transmit Diversity Scheme

This chapter of the thesis is based on the UAV-assisted OWC which provides a promising solution to cost-efficient and reliable wireless communications. UAV-assisted OWCs can provide improved communication over fixed-to-fixed OWC networks, and due to the mobility of UAVs, it can configure a flexible communication environment according to surrounding conditions and can provide a promising solution for wireless fronthaul and backhaul. For the successful UAV-assisted OWC, transmitting the data from the ground station is important. We focus on improving the ground-to-UAV optical link using maximal selection transmit diversity (MSTD).

2.1 UAV-assisted OWC

OWC is attracting attention as a B5G and 6G communication method because it has features such as unlicensed band, ultra-wide band, electromagnetic interference irrelevant, directional communication, long-distance transmission, and line-of-sight-based security communication [2].

UAV is a very usable vehicle that has been found effective for civil and military purposes. UAV provides a promising solution to cost-efficient and reliable wireless communications. For the mobility of the UAV, one of the advantages of UAV-assisted OWC is the construction of a flexible network. It can be used in places where wireless communication traffic is steeply and temporarily increased, such as performance halls, stadiums, conference halls, and multi-use facilities, as well as in disaster situations where communication infrastructures are damaged [11].

In emergency communication network establishment, UAV-assisted OWC has advantages of simpler application, lower cost, and less communication delay than artificial satellites [12].

Despite these advantages, there are some challenges to be solved. For example, aerosol absorption and scattering caused by fog, snow, and rain may affect performance degradation. In addition, turbulence-induced fading is one of the main cause of performance impairment at OWC. It is caused by atmospheric turbulence that is due to the variations in the air refractive index with temperature and atmospheric turbulence caused signal fading [13][14].

2.2 Maximal Selection Transmit Diversity

We study the maximal selection transmit diversity (MSTD) scheme with a strict power budget imposed to solve the negative effect of optical communication channels on the ground-to-UAV link. MSTD means selecting the transmitter antenna with the highest power among several antennas to communicate with one receiver. This study considers several transmitters which are an optical array and one UAV equipped with one receiver in the distant sky. The turbulence-induced fading is assumed to obey the log-normal distribution. We calculate the largest order statistics of the channel gain for the wireless communication link based on MSTD [15].

2.3 System Model

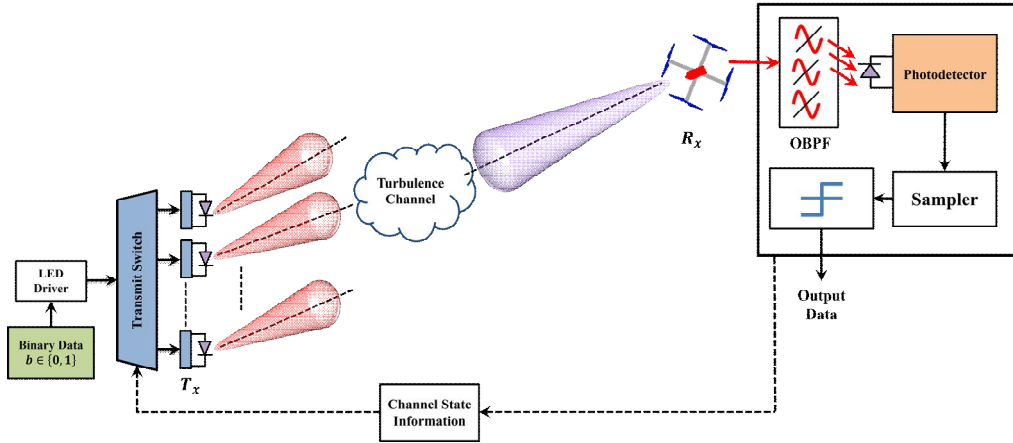


Figure 2.1. Link geometry of ground-to-UAV optical communication.

The link geometry of MSTD-based ground-to-UAV optical communication is shown in Figure 2.1. Since the turbulence fading is a slow time-varying process, we assume that the channel condition information is available at the transmitter side. We consider that the optical array with L laser sources is pointing toward the UAV equipped with the receiver. At the transmitter, laser sources are assumed to be intensity-modulated and at the receiver side, UAV is assumed to be an ideal non-coherent receiver. To ignore the background noise mean power, constant bias is subtracted. The output of the receiver corresponding to the l th symbol duration, i.e., $[(l-1)T_s, lT_s]$, with T_s being the symbol duration, can be written as

$$y[l] = Rhs[l] + n[l], \quad (2.1)$$

where h represents the optical channel gain coefficient accounting for the attenuation and absorption, $n[l]$ is the noise, $s[l]$ is the information data, and R denotes the responsivity of the detector. Assuming log-normal distributed turbulence fading, the probability density function (PDF) of the optical channel from ground-to-UAV is given by [16]

$$f_h(h) = \exp\left(\frac{-\theta_{FOV}^2}{2\sigma_\theta^2}\right)\delta(h) \quad (2.2)$$

$$+ C_e\left(1 - \exp\left(\frac{-\theta_{FOV}^2}{2\sigma_\theta^2}\right)\right)h^{(\gamma_{gu}^2-1)}Q\left(\frac{\ln\left(\frac{h}{A_0h_e}\right) + C_d}{2\sigma_{\ln h_a}}\right)$$

where θ_{FOV} is the receiver FOV angle, σ_θ^2 is the variance of the UAV orientation deviations, and $\sigma_{\ln h_a}^2$ represents the variance of the log-irradiance. h_l is the atmospheric attenuation. A_0 is the maximal fraction of the collected intensity. $C_e = \frac{\gamma_{gu}^2}{(A_0h_l)^{\gamma_{gu}^2}}\exp[2\sigma_{\ln h_a}^2\gamma_{gu}^2(1+\gamma_{gu}^2)]$ and $\gamma_{gu}^2 = \frac{w_{zeq}^2}{4\sigma_{pq}^2}$. w_{zeq} is the equivalent beam waist and σ_{pq}^2 is the sum of the variances of the ground station position and the UAV position. Utilizing the identity [17, eq. 12] into (2.2) and apply some mathematical manipulations, (2.2) can be rewritten as

$$f_h(h) = \exp\left(\frac{-\theta_{FOV}^2}{2\sigma_\theta^2}\right)\delta(h) + C_e\left(1 - \exp\left(\frac{-\theta_{FOV}^2}{2\sigma_\theta^2}\right)\right) \quad (2.3)$$

$$\times h^{(\gamma_{gu}^2-1)}\frac{1}{2}\left(1 - \operatorname{erf}\left(\frac{\ln\left(\frac{h}{A_0h_e}\right) + C_d}{2\sigma_{\ln h_a}}\frac{1}{\sqrt{2}}\right)\right)$$

Using the identities [18, eq. 1.512.1] and [17, eq. 12] the PDF of the channel gain can be obtained as shown in (2.4). Following the result obtained in (2.4), the CDF of the channel gain can be obtained using $F_h(h) = \int_0^h f_a(a)da$, where $f_a(a)$ is the PDF of the channel gain derived in (2.4).

$$\begin{aligned}
f_h(h) &= \exp\left(\frac{-\theta_{FOV}^2}{2\sigma_\theta^2}\right)\delta(h) + \frac{C_e}{2}\left(1 - \exp\left(\frac{-\theta_{FOV}^2}{2\sigma_\theta^2}\right)\right)h^{(\gamma_{gu}^2 - 1)} \\
&\quad - \frac{C_e}{2\sqrt{\pi}}\left(1 - \exp\left(\frac{-\theta_{FOV}^2}{2\sigma_\theta^2}\right)\right)h^{(\gamma_{gu}^2 - 1)} \\
&\quad \times G_{1,2}^{1,1}\left\{\left(\sum_{K=1}^{\infty} \frac{(-1)^{(K+1)}(h - A_0 h_e)^K}{K(A_0 h_e)^K \sqrt{2} 2\sigma_{\text{Lnh}_a}} + \frac{C_d}{\sqrt{2} 2\sigma_{\text{Lnh}_a}}\right)^2 \middle| \begin{matrix} 1 \\ \frac{1}{2} 0 \end{matrix}\right\}
\end{aligned} \tag{2.4}$$

$$\begin{aligned}
F_h(h) &= \int_0^h \exp\left(\frac{-\theta_{FOV}^2}{2\sigma_\theta^2}\right)\delta(a)da + \int_0^h \frac{C_e}{2}\left(1 - \exp\left(\frac{-\theta_{FOV}^2}{2\sigma_\theta^2}\right)\right)a^{(\gamma_{gu}^2 - 1)da} \\
&\quad - \frac{C_e}{2\sqrt{\pi}}\left(1 - \exp\left(\frac{-\theta_{FOV}^2}{2\sigma_\theta^2}\right)\right) \\
&\quad \times \int_0^h a^{(\gamma_{gu}^2 - 1)} \times G_{1,2}^{1,1}\left\{\left(\sum_{K=1}^{\infty} \frac{(-1)^{(K+1)}(h - A_0 h_e)^K}{K(A_0 h_e)^K \sqrt{2} 2\sigma_{\text{Lnh}_a}} + \frac{C_d}{\sqrt{2} 2\sigma_{\text{Lnh}_a}}\right)^2 \middle| \begin{matrix} 1 \\ \frac{1}{2} 0 \end{matrix}\right\} da
\end{aligned} \tag{2.5}$$

2.3.1. CDF of the largest Order Statistics

We assume that the optical channels encountered between the transmitters and the UAV are independent and identically distributed random variables. Therefore, the CDF of the largest order statistics, h_{\max} , can be obtained as [19]

$$\begin{aligned}
F_{h_{\max}}(h_{\max}) &= P_r[h_{\max} \leq h] \\
&= P_r\left[\begin{matrix} h_l \\ \forall l = \{1, \dots, l, \dots, L\} \end{matrix} \leq h\right] = [F_h(h)]_L
\end{aligned} \tag{2.6}$$

Utilizing (2.6), we obtain the PDF of the largest order statistics $f_{h_{\max}}(h_{\max})$ using

$$f_{h_{\max}}(h_{\max}) = L[F_h(h)]^L f_h(h) \quad (2.7)$$

2.3.2. Average Bit Error Rate

For the analysis purpose, first we define the signal to noise ratio (SNR) for the given system. Let P_T be the total power budget constraint imposed. Following (2.1), the instantaneous received electrical SNR at the UAV can be written as

$$\xi = \frac{(RP_T)^2 h^2}{L^2 N_0} \quad (2.8)$$

It is important to note that, the proposed system is power efficient. As illustrated in (2.8), a strict power budget is imposed and thus the average power assigned to each branch is always P_T/L . We assume non-return-to-zero OOK modulated signal. The conditional BER can then be obtained as $P_e(\xi | h_{\max}) = \frac{1}{2} \operatorname{erfc}\left(\frac{1}{2\sqrt{2}} \sqrt{E[\xi]h_{\max}^2}\right)$ where $\operatorname{erfc}(\cdot)$ denotes the complementary error function. $E[\cdot]$ is the expectation operation. The average BER can then readily be obtained as

$$P_{Avg} = \int_0^{\infty} P_e(\xi | h_{\max}) f_{h_{\max}}(h_{\max}) dh_{\max}. \quad (2.9)$$

2.4 Results and Analysis

With the hovering UAV equipped with the receiver, the simulation parameters are illustrated in Table 2.1.

Table 2.1. Simulation parameters [16].

parameter	value
Optical wavelength	1550 nm
Aperture radius	5 cm
Receiver quantum efficiency	0.60
$\sigma_{Lnh_a}^2$	0.1
σ_p	25 cm
σ_g	25 cm

Figure 2.2 represents the BER performance of the MSTD scheme for the ground-to-UAV link relative to the average received SNR for different turbulence strengths. This result shows that the MSTD scheme for the UAV-assisted OWC is effective to eliminate the impact of severe path loss. We can note that the application of MSTD significantly increases the performance, irrespective of the turbulence strength. For example, when the index of refraction structure parameter C_n^2 is equal to $8.4 \times 10^{-15} \text{m}^{-2/3}$ and the received SNR is 20 dB, the BER decreases approximately by an order of 10 when the elements in the optical array are increased from $L = 1$ to $L = 3$.

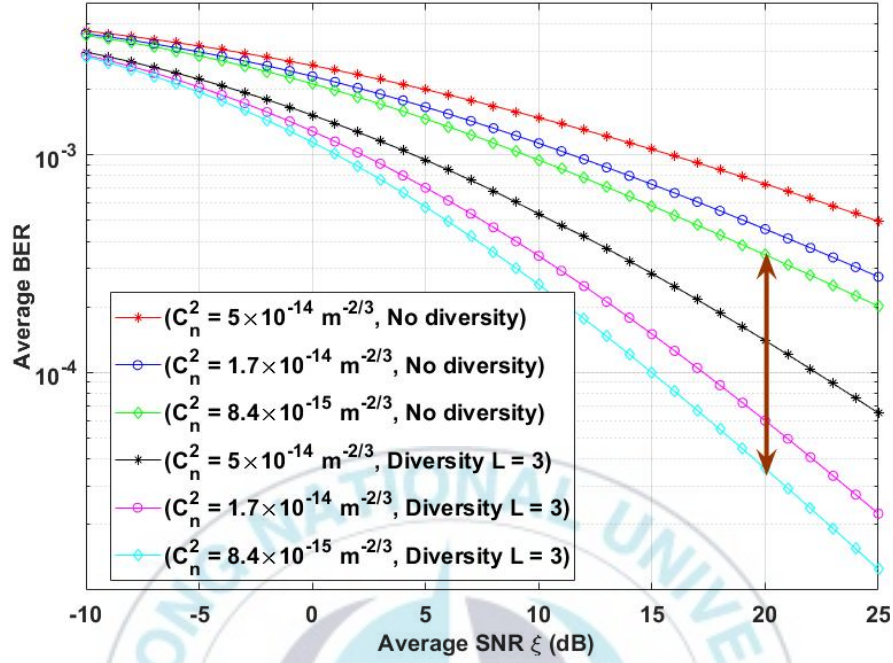


Figure 2.2. BER relative to the average received SNR for different turbulence strength.

Figure 2.3 represents the BER performance of the MSTD scheme for the ground-to-UAV link relative to the link range for different turbulence strengths. The total power budget is set to 12 dBm. It is shown that the proposed MSTD based on the selection of the optical path with a larger value of the channel gain extracts full diversity and provides better performance, compared to the conventional ground-to-UAV system with single branch.

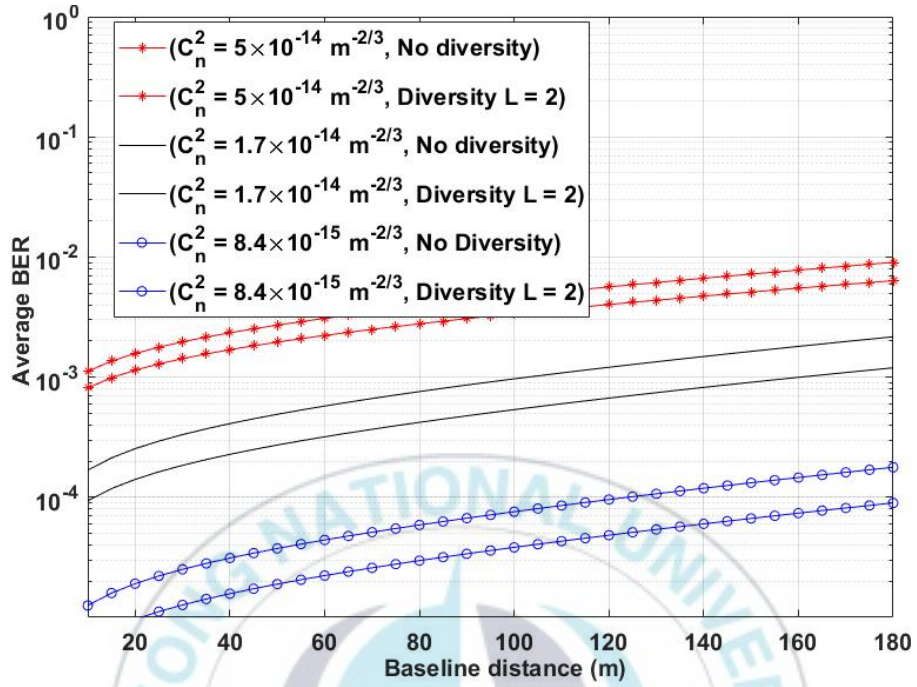


Figure 2.3. BER relative to the link range for different turbulence strength.

3. Switch-and-Stay Combining over Correlated Channels

The target of this study is to develop the performance of UAV-assisted OWC using switch-and-stay combining technique in ground-to-UAV communication link. We consider turbulence-induced fading that is the major channel impairments in optical communication. We use frequency-shift keying sub-carrier intensity modulation. To verify the effectiveness of the proposed system, average bit error rate is simulated.

3.1 FSK-SIM with Correlated Branches

To mitigate the channel impairments due to turbulence-induced fading in ground-to-UAV communication link, we propose a novel transmission technique that is composed of frequency-shift keying subcarrier intensity modulation equipped with switch-and-stay combining (SSC) diversity reception. SSC is a selection combining in diversity schemes with two receiving antennas. It operates to maintain the sufficient link performance. If the activating link has sufficient link performance, it maintains the connection regardless of the quality of the remaining branch [20].

For more realistic analysis, we model the propagation channel as a correlated channel and the turbulence-induced fading is modeled as gamma-gamma distribution.

3.2 System Model

The received signal at the i th branch is quantified as

$$y_i = SHP_t I_i + w_n, \quad i = 1, 2, \quad (3.1)$$

where S represents the responsivity in A/W , H is the deterministic path loss, and P_t is the transmit power. I_i is a random variable following the gamma-gamma distribution and denotes the turbulence-induced fading. w_n represents the additive white Gaussian noise with power spectral density represented by N_0 . Following (3.1), we define the instantaneous SNR at the i th branch as

$$X_i = \frac{(SH P_t)^2 I_i^2}{N_0} \quad (3.2)$$

We normalized the fading such that $E[I_i^2] = 1, \forall i \in \{1, 2\}$, it yields the average received SNR \bar{X} to be defined as

$$\bar{X} = \frac{(SH P_t)^2}{N_0} \quad (3.3)$$

The PDF of $I_i, i \in \{1, 2\}$ is given by

$$f_{I_i}(I_i) = \frac{2(pq)^{\left(\frac{p+q}{2}\right)} I^{\frac{p+q}{2}-1}}{\Gamma(p)\Gamma(q)} K_{p-q}(2\sqrt{pqI}), \quad i = 1, 2 \quad (3.4)$$

where $K_{p-q}(\cdot)$ is the modified Bessel function of the second kind and order $p-q$. Utilizing (3.2), (3.3), and (3.4), and applying the Jacobean transformation, the PDF of the instantaneous SNR X is derived as

$$f_{\chi_i}(\chi_i) = \frac{(pq)^{\binom{p+q}{2}}}{2\Gamma(p)\Gamma(q)} \frac{\chi_i^{\frac{p+q}{4}-1}}{\chi_i^{\frac{p+q}{4}}} G_{0,2}^{2,0} \left(pq \sqrt{\frac{\chi}{\chi}} \left| \frac{p-q}{2}, -\frac{p-q}{2} \right. \right) \quad (3.5)$$

where $G_{s,t}^{u,v}(\cdot)$ denotes the Meijer G-function.

3.3 Performance Analysis

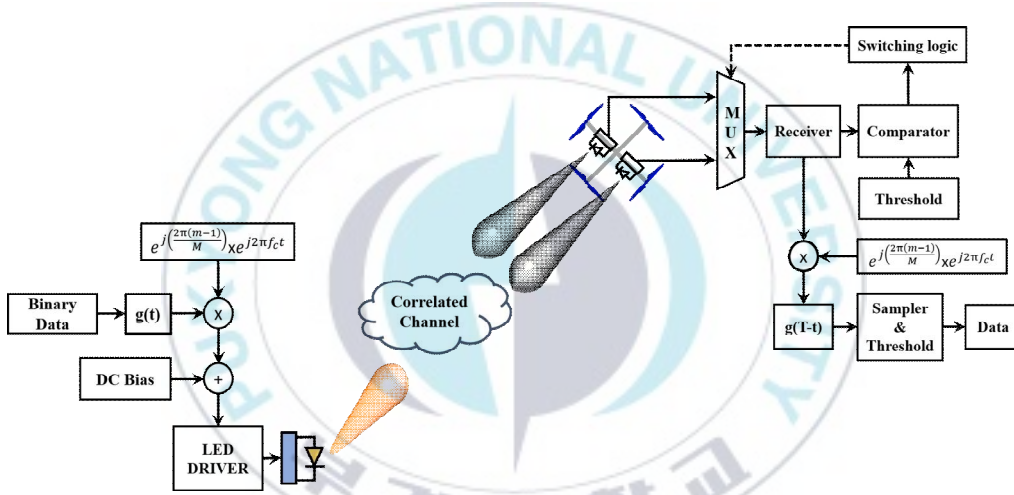


Figure 3.1. Switch-and-stay combining equipped with subcarrier frequency-shift keying for ground-to-UAV optical link.

We consider frequency shift keying sub-carrier intensity modulation with correlated branches. The instantaneous BER conditioned on the instantaneous received SNR is then given by

$$P_e = \frac{1}{2\sqrt{\pi}} G_{1,2}^{2,0} \left(\frac{\chi}{2} \left| 0, \frac{1}{2} \right. \right) \quad (3.6)$$

Let $f_{SSC}(X)$ be the PDF of the final SNR obtained at the multiplexer output, as illustrated in Figure 3.1. Averaging over the distribution of $f_{SSC}(X)$, the average BER is given by

$$\bar{P}_e = \frac{1}{2} \int_0^\infty G_{1,2}^{2,0} \left(\frac{\chi}{2} \middle| 0, \frac{1}{2} \right) f_{SSC}(\chi) d\chi \quad (3.7)$$

The $f_{SSC}(X)$ is defined as

$$f_{SSC}(X) = \begin{cases} g_{\chi(\chi_{Th}, \chi)}, & \chi \leq \chi_{Th} \\ f_{\chi}(\chi) + g_{\chi(\chi_{Th}, \chi)}, & \chi > \chi_{Th} \end{cases} \quad (3.8)$$

where $g_{\chi(\chi_{Th}, \chi)}$ is given by

$$g_{\chi(\chi_{Th}, \chi)} = \int_0^{\chi_{Th}} f_{\chi_1, \chi_2}(\chi, \chi_2) d\chi_2 \quad (3.9)$$

Substituting $f_{\chi_1, \chi_2}(\chi, \chi_2)$ into (3.9), and applying simple mathematical manipulations, we obtained

$$\begin{aligned} g_{\chi(\chi_{Th}, \chi)} &= \left(\frac{1}{2} \right)^2 \frac{(1-\rho^2)^q}{[\Gamma(p)]^2 \Gamma(q)} \sum_{i=0}^{\infty} \left(\frac{\Xi}{\sqrt{\chi}} \right)^{(p+q+i)} \frac{\rho^{2i}}{\Gamma(q+i)i!} \\ &\times \chi^{\frac{(p+q+i-4)}{4}} G_{0,2}^{2,0} \left(\Xi \sqrt{\frac{\chi}{\chi}} \middle| \frac{q+i-p}{2}, -\frac{q+i-p}{2} \right) \\ &\times \int_0^{\chi_{Th}} \chi_2^{\frac{(p+q+i-4)}{4}} G_{0,2}^{2,0} \left(\Xi \sqrt{\frac{\chi}{\chi}} \middle| \frac{q+i-p}{2}, -\frac{q+i-p}{2} \right) d\chi_2 \end{aligned} \quad (3.10)$$

Utilizing the identity [17, eq. (26)] and applying some mathematical

manipulations, the integral in (3.10) can be solved as

$$\begin{aligned}
g_{\chi(\chi_{Th}, \chi)} &= \left(\frac{1}{2}\right)^2 \frac{(1-\rho^2)^q}{[\Gamma(p)]^2 \Gamma(q)} \sum_{i=0}^{\infty} \left(\frac{\Xi}{\sqrt{\chi}}\right)^{(p+q+i)} \frac{\rho^{2i}}{\Gamma(q+i)i!} \\
&\times \chi^{\frac{(p+q+i-4)}{4}} G_{0,2}^{2,0} \left(\Xi \sqrt{\frac{\chi}{\chi}} \left| \begin{matrix} - \\ q+i-p, -q+i-p \end{matrix} \right. \right) \\
&\times \left(\Xi \sqrt{\frac{\chi_{Th}}{\chi}} \right)^{\frac{(p+q+i)}{2}} G_{1,3}^{2,1} \left(\Xi \sqrt{\frac{\chi}{\chi}} \left| \begin{matrix} 1 - \frac{p+q+i}{4} \\ q+i-p, -q+i-p, -\frac{p+q+i}{4} \end{matrix} \right. \right)
\end{aligned} \tag{3.11}$$

Eq. (3.11) can further be simplified by utilizing the identity [21, eq. (8.2.2.15)] as shown in (3.12).

$$\begin{aligned}
g_{\chi(\chi_{Th}, \chi)} &= \left(\frac{1}{2}\right)^2 \frac{(1-\rho^2)^q}{[\Gamma(p)]^2 \Gamma(q)} \sum_{i=0}^{\infty} \frac{\rho^{2i} \chi^{-1}}{\Gamma(q+i)i!} \\
&\times G_{0,2}^{2,0} \left(\Xi \sqrt{\frac{\chi}{\chi}} \left| \begin{matrix} - \\ q+i, p \end{matrix} \right. \right) \\
&\times G_{1,3}^{2,1} \left(\Xi \sqrt{\frac{\chi}{\chi}} \left| \begin{matrix} 1 + \frac{q+i+p}{4} \\ q+i, p, \frac{q+i+p}{4} \end{matrix} \right. \right)
\end{aligned} \tag{3.12}$$

3.3.1. Average BER when $\chi \leq \chi_{Th}$

Utilizing (3.8) and (3.10), and using the identity [21, eq. (8.2.2.15)], the instantaneous BER of the proposed system when $\chi \leq \chi_{Th}$ is given by

$$\begin{aligned}
\bar{P}_e | \chi < \chi_{Th} &= \frac{(1-\rho^2)^q}{16\sqrt{\pi}[\Gamma(p)]^2\Gamma(q)} \sum_{i=0}^{\infty} \frac{\rho^{2i}}{\Gamma(q+i)i!} \\
&\times G_{1,3}^{2,1} \left(\Xi \sqrt{\frac{\chi_{Th}}{\chi}} \middle| \begin{matrix} 1 + \frac{q+i+p}{4} \\ q+i, p, \frac{q+i+p}{4} \end{matrix} \right) \\
&\times \int_0^{\infty} G_{1,2}^{2,0} \left(\frac{\chi}{2} \middle| \begin{matrix} 0 \\ -1, -\frac{1}{2} \end{matrix} \right) G_{0,2}^{2,0} \left(\Xi \sqrt{\frac{\chi}{\chi}} \middle| \begin{matrix} - \\ q+i, p \end{matrix} \right) d\chi
\end{aligned} \tag{3.13}$$

With the aid of the identities [17, eq. (21)] and [17, eq. (22)], the closed-form expression for $\bar{P}_e |_{\chi < \chi_{Th}}$ is derived as shown in (3.14).

3.3.2. Average BER when $\chi > \chi_{Th}$

Utilizing (3.5), (3.8), and (3.10), the average BER when $\chi > \chi_{Th}$ can be written as shown in (3.15). Using the identity [21, eq. (8.2.2.15)] and [17, eq. (21)], the average BER when $\chi > \chi_{Th}$ is derived as shown in (3.16).

$$\begin{aligned}
\bar{P}_e | \chi < \chi_{Th} &= \frac{(1-\rho^2)^q}{16\sqrt{\pi}[\Gamma(p)]^2\Gamma(q)} \sum_{i=0}^{\infty} \frac{\rho^{2i}}{\Gamma(q+i)i!} \\
&\times G_{1,3}^{2,1} \left(\Xi \sqrt{\frac{\chi_{Th}}{\chi}} \middle| \begin{matrix} 1 + \frac{q+i+p}{4} \\ q+i, p, \frac{q+i+p}{4} \end{matrix} \right) \\
&\times G_{2,5}^{4,2} \left(\frac{\Xi^2}{8\chi} \middle| \begin{matrix} 1, \frac{1}{2} \\ \frac{q+i}{2}, \frac{q+i+1}{2}, \frac{p}{2}, \frac{p+1}{2}, 0 \end{matrix} \right)
\end{aligned} \tag{3.14}$$

$$\begin{aligned}
\bar{P}_e | \chi > \chi_{th} &= \frac{(1-\rho^2)^q}{16\sqrt{\pi}[\Gamma(p)]^2\Gamma(q)} \sum_{i=0}^{\infty} \frac{\rho^{2i}}{\Gamma(q+i)i!} \quad (3.15) \\
&\times G_{1,3}^{2,1} \left(\Xi \sqrt{\frac{\chi_{th}}{\chi}} \left| \begin{matrix} 1 + \frac{q+i+p}{4} \\ q+i, p, \frac{q+i+p}{4} \end{matrix} \right. \right) \\
&\times G_{2,5}^{4,2} \left(\frac{\Xi^2}{8\chi} \left| \begin{matrix} 1, \frac{1}{2} \\ \frac{q+i}{2}, \frac{q+i+1}{2}, \frac{p}{2}, \frac{p+1}{2}, 0 \end{matrix} \right. \right) \\
&+ \frac{1}{4\sqrt{\pi}} \frac{(pq)^{\frac{p+q}{2}}}{\Gamma(p)\Gamma(q)} \int_0^{\infty} \frac{\chi^{\frac{p+q-1}{4}}}{\chi^{\frac{p+q}{4}}} G_{1,2}^{2,0} \left(\frac{\chi}{2} \right)
\end{aligned}$$

$$\begin{aligned}
\bar{P}_e | \chi > \chi_{th} &= \frac{(1-\rho^2)^q}{16\sqrt{\pi}[\Gamma(p)]^2\Gamma(q)} \sum_{i=0}^{\infty} \frac{\rho^{2i}}{\Gamma(q+i)i!} \quad (3.16) \\
&\times G_{1,3}^{2,1} \left(\Xi \sqrt{\frac{\chi_{th}}{\chi}} \left| \begin{matrix} 1 + \frac{q+i+p}{4} \\ q+i, p, \frac{q+i+p}{4} \end{matrix} \right. \right) \\
&\times G_{2,5}^{4,2} \left(\frac{\Xi^2}{8\chi} \left| \begin{matrix} 1, \frac{1}{2} \\ \frac{q+i}{2}, \frac{q+i+1}{2}, \frac{p}{2}, \frac{p+1}{2}, 0 \end{matrix} \right. \right) \\
&+ \frac{1}{\pi^{\frac{3}{2}}} \frac{2^{\frac{(3p+q-4)}{2}}}{\Gamma(p)\Gamma(q)} G_{2,5}^{4,2} \left(\frac{pq}{2\sqrt{2\chi}} \right) \left| \begin{matrix} 1, \frac{p+q-1}{2} \\ \frac{3q-p}{2} \end{matrix} \right.
\end{aligned}$$

3.4 Results and Discussion

The optical wavelength is set to 532 nm. The responsivity S is set to 0.4. For good statistical average, the random variable I is generated with 3000 realization. Unless otherwise stated, the detection threshold χ_{th} is set to 5 dB and the correlation coefficient is set to 0.5.

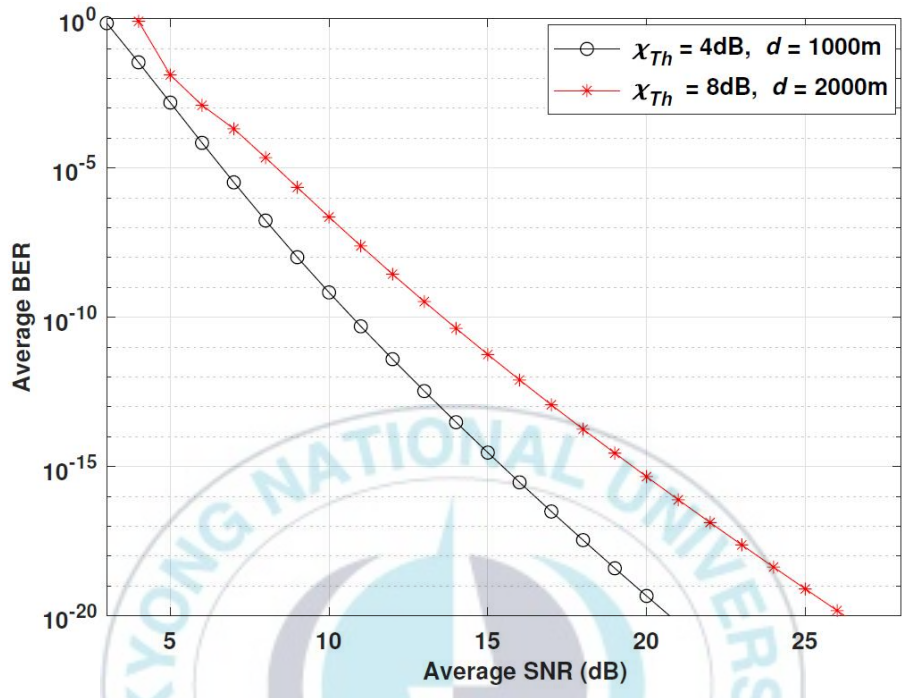


Figure 3.2. Average BER performance relative to the average received SNR for different threshold and link range values.

Figure 3.2 depicts the average BER performance relative to the average received SNR for different threshold and link range values. As we can expected, according to increasing distance, the performance degrades. In addition, the important observation is that the performance improves when detection threshold reduces at the same average SNR. This can mean that lower the detection threshold, the more frequent the switching occurs. Therefore, it increases the probability of selecting the best branches.

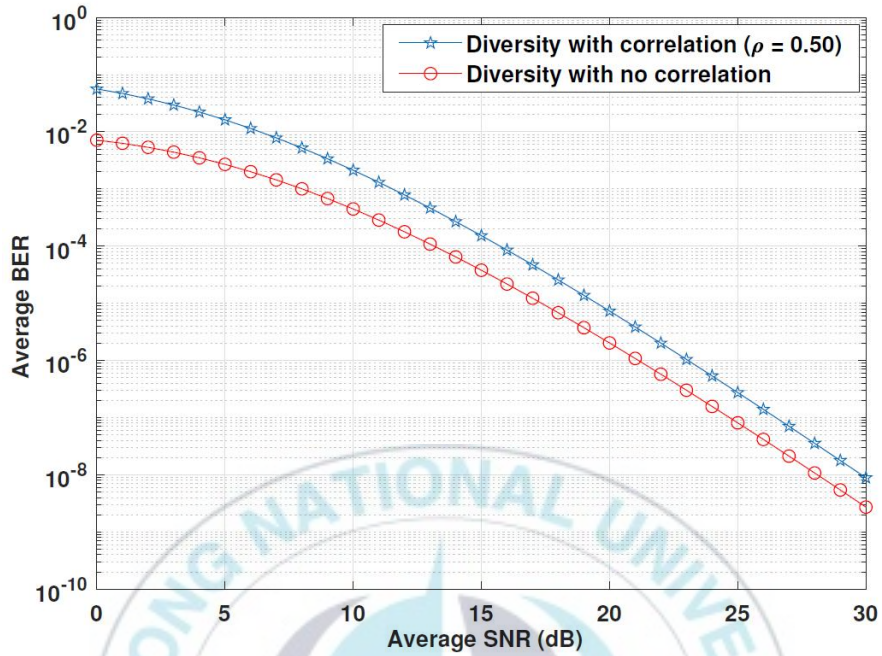


Figure 3.3. Impact of correlation on sub-carrier intensity modulated frequency shift keying equipped with switch-and-stay combining diversity technique.

Figure 3.3. depicts that impact of correlation on the performance of the proposed system. As the correlation increases, the performance degrades. For example, at the average received SNR of 10 dB, as the channel correlation increases from 0 to 0.5, the BER increases by 4 times.

4. Impact of Hovering on Laguerre–Gaussian Beam Propagation

The target of this study is to investigate the impact of UAV hovering on Laguerre–Gaussian beam propagation for UAV–to–ground optical communications. Hovering UAV slightly keeps moving in all directions due to the wind. This movement causes misalignment between the transmitter and receiver at the OWC that needs to establish an LOS link. We model the hovering UAV and simulate the impact of the hovering UAV on Laguerre–Gaussian beam propagation.

4.1 Hovering Impact on UAV–to–Ground Links

We investigate UAV–to–ground OWC in this study. OWC has the characteristic that the LOS link needs to be configured but the hovering UAV moved by wind steadily disturbs the establishment of alignment between the transmitter and the receiver. It is required to investigate the loss due to hovering.

4.2 Laguerre–Gaussian Beam Propagation

We also consider the Laguerre–Gaussian beam. This paper is devoted to exploring the potential of employing Laguerre–Gaussian beam carrying helical phase structure for UAV–to–ground communications under hovering conditions. Laguerre–Gaussian has the phase singularity which is the twist of the wavefront during the transmission, thereby forming vortex waves [22].

4.3 System Model

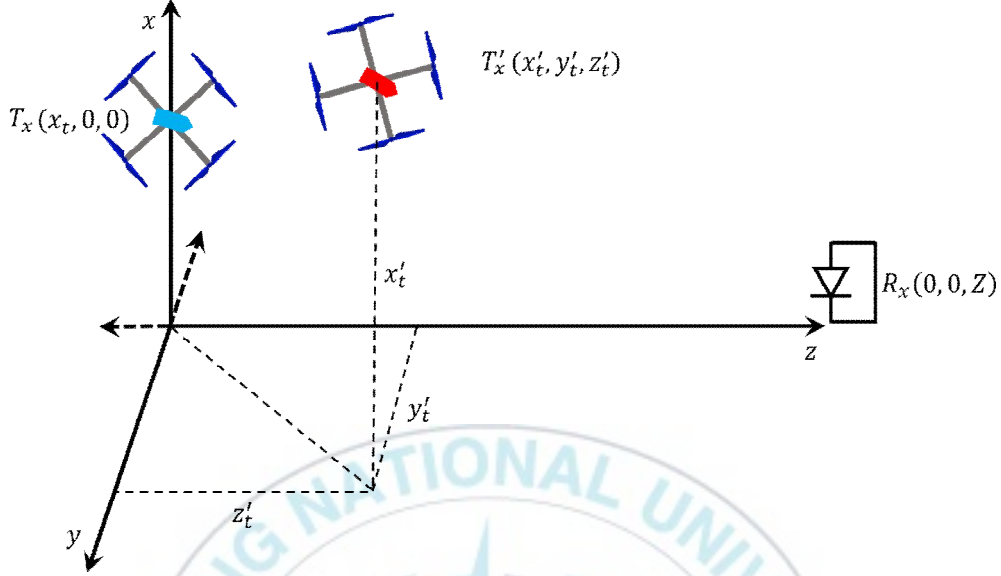


Figure 4.1. UAV-to-ground optical communication link geometry.

We consider the UAV-to-ground optical link geometry, as illustrated in Figure 4.1. In this figure, hovering UAV equipped with transmitter is over the sky and the receiver is on the ground. In UAV-to-ground optical communication links, the channel characteristic is determined by LOS propagation with high mobility. We also consider the right-handed coordinate system, with the positive X-axis points in the upward direction. The receiver coordinates are $(0, 0, z)$. The initial UAV coordinates are $(x_t, 0, 0)$. A hovering UAV coordinates after some time from the initial UAV are (x'_t, y'_t, z'_t) .

4.3.1. Hovering Loss

At the transmitter, We consider a Laguerre-Gaussian beam. The helical phase structure is represented by the phase term $\exp(il\phi)$, where l denotes the topological charge and ϕ is the azimuthal angle. The radial intensity distribution of the transmitted Laguerre-Gaussian beam

is given by [22]

$$\begin{aligned}
I(r, \phi, z) &= \alpha \sqrt{\frac{p!}{\pi(p + \|l\|)!}} \frac{1}{w(z)} \left(\frac{\sqrt{x^2 + y^2} \sqrt{2}}{w(z)} \right)^{\|l\|} \exp\left(-\frac{x^2 + y^2}{w^2(z)}\right) \\
&\times L_p^{\|l\|} \left(\frac{2(x^2 + y^2)}{w^2(z)} \right) \exp\left(-i \frac{\pi(x^2 + y^2)}{\lambda R(z)}\right) \\
&\times \exp(i(\|l\| + 2p + 1)\psi(z)) \exp(-il\phi)
\end{aligned} \tag{4.1}$$

with

$$R(z) = z \left[1 + \left(\frac{\pi w_l^2}{\lambda z} \right)^2 \right] \tag{4.2}$$

$$w(z) = w_l \sqrt{1 + \left(\frac{z}{zR} \right)^2} \tag{4.3}$$

where the term $\alpha \sqrt{\frac{p!}{\pi(p + \|l\|)!}}$ is a normalized constant, p is the radial index which represents the number of radial nodes in the intensity distribution.

Considering the Laguerre-Gaussian beam, the misalignment loss at the receiver due to the hovering UAV can then readily be obtained as (4.4)

$$L_H = \alpha \sqrt{\frac{p!}{\pi(p + \|l\|)!}} \frac{1}{w(z)} \exp[(i\|l\| + 2p + 1)\psi(z)] \exp(-il\phi)$$

$$\begin{aligned}
& \times \int_{-\frac{D}{2}}^{\frac{D}{2}} \int_{-\sqrt{\frac{D^2}{4}-y^2}}^{\sqrt{\frac{D^2}{4}-y^2}} \left\{ \left(\frac{\sqrt{2[(x+x_s)^2+(y+y_s)^2]}}{w(z)} \right)^{\|l\|} \right. \\
& \times \exp \left[-\frac{(x+x_s)^2+(y+y_s)^2}{w^2(z)} \right] \left. \right\} L_p^{\|l\|} \left\{ \frac{2[(x+x_s)^2+(y+y_s)^2]}{w^2(z)} \right\} \\
& \times \exp \left[-i\pi \frac{(x+x_s)^2+(y+y_s)^2}{\lambda R(z)} \right] \left. \right\} dx dy
\end{aligned} \tag{4.4}$$

We want to emphasize that the intensity profile of the received Laguerre-Gaussian beam looks like a narrow window with most of the received power concentrated in a narrow ring. The radius of the ring with maximum received intensity can then readily be obtained using $d \| L_H(r, \phi, z) \|^2 / dr = 0$.

4.4 Results and Discussion

Table 4.1. Simulation parameters.

Parameter	Value
Optical wavelength	530 nm
Area of the detector	1.77 cm ²
Receiver quantum efficiency	0.30

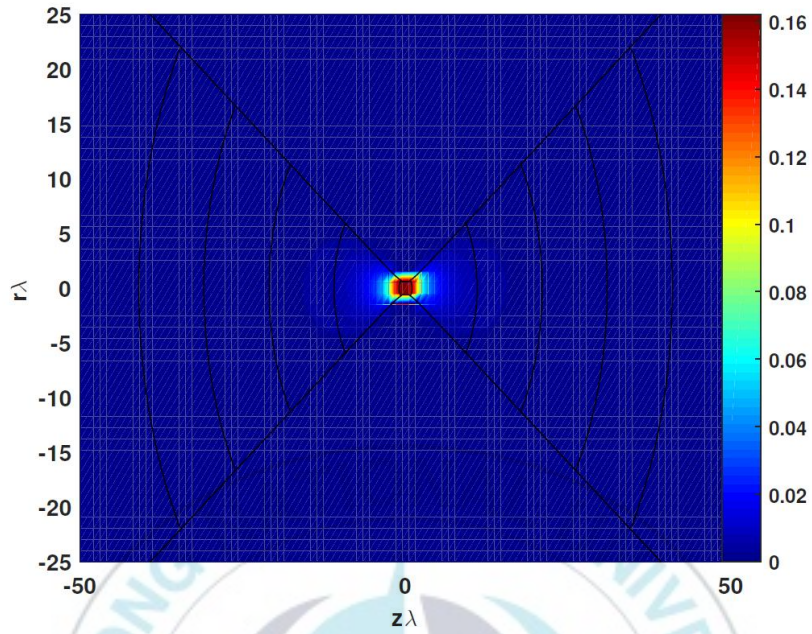


Figure 4.2. Transmitted beam

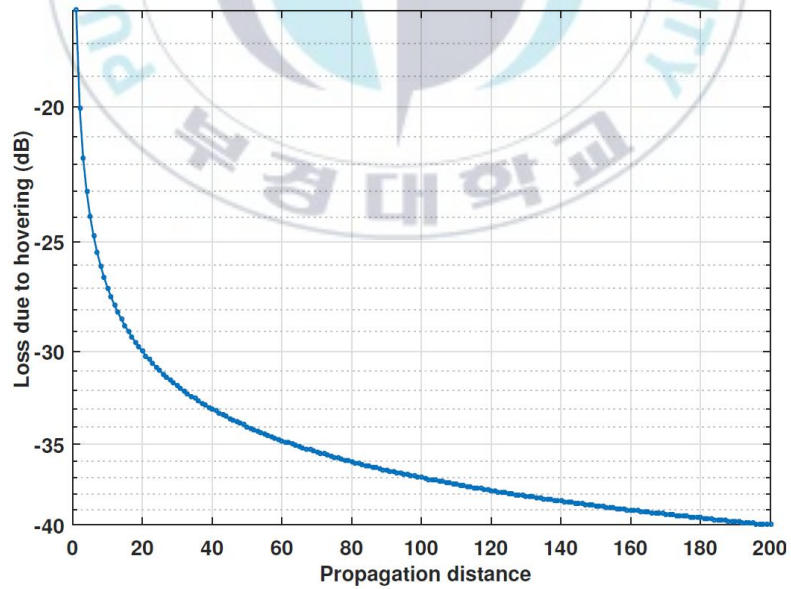


Figure 4.3. Intensity loss due to hovering relative to the propagation distance.

In the UAV-to-ground optical communication link geometry, the simulation parameters are illustrated in Table 4.1. The profile distribution of the transmitted Laguerre-Gaussian beam is illustrated in Figure 4.2. Based on different spiral phase distribution, the mode of transmitted beam can be identified intuitively. Distortion of its phasefront is occurred by the propagation of the Laguerre-Gaussian beam through the proposed optical communication channel. At the detector, the wave becomes to a ray with both distorted phase profile and amplitude. The propagation intensity loss relative to the propagation distance is illustrated in Figure 4.3. The misalignment, which is occurred by the hovering UAV, between the transmitter and the receiver results in power loss and inter-channel crosstalk. Moreover, the distorted phasefront leads to power leakage to neighboring modes. The leakage in the transmitted optical energy leads to both power loss and crosstalk among different modes. Moreover, a limited detector aperture size results in an additional loss in the received intensity.

5. Link Connectivity in UAV Optical Ad-Hoc Network

In this chapter, we investigate the connectivity of the UAVs in a one-dimensional ad-hoc optical network. For communication between two very distant points in communication using UAV, not only UAV-to-ground, ground-to-UAV but also UAV-to-UAV link that communicates between UAVs is required due to the limitation of the maximum transmission distance. Since UAVs can freely move, the distance between UAVs can be varied. Since the probability of connectivity between UAVs also change as the distances change, we investigated the probability of connectivity according to the arrangement of UAVs and the maximum transmission distance.

5.1 UAV-to-UAV Communication

Free space optical communication is attracting attention as a next-generation communication after RF. One of the challenges that optical communication has to overcome is how to configure LOS links in cities with many obstacles. When trying to transmit optical signals from a building roof to a building roof that is far away, if a large building in the middle is blocking it, a repeater must be installed in that building. As one of the ways to overcome this, communication relay through UAV is attracting attention. If only one UAV is launched in the sky, no matter how many obstacles are on the ground, LOS link can be formed and signals can be transmitted directly through the UAV [10].

However, in order to communicate with a very distant area, it is necessary to communicate between UAVs using several UAVs. One of the problems that can arise at this time is that since the UAV can

move freely, it may exceed the maximum transmission range of the signal. In this chapter, we will look at connectivity in UAV ad-hoc optical networks.

5.2 Connectivity in One-dimensional UAV Ad-hoc Network

In this paper, we consider randomly distributed UAVs that obey the Poisson point process in one-dimensional space. We analyze the issue of connectivity in communication between randomly distributed UAVs. Not only the connectivity issue between neighboring UAVs, but also the connectivity between the second and third neighboring UAVs and the end-to-end connectivity were mathematically analyzed. In addition, the impact of UAV density and threshold range is also considered to analyze.

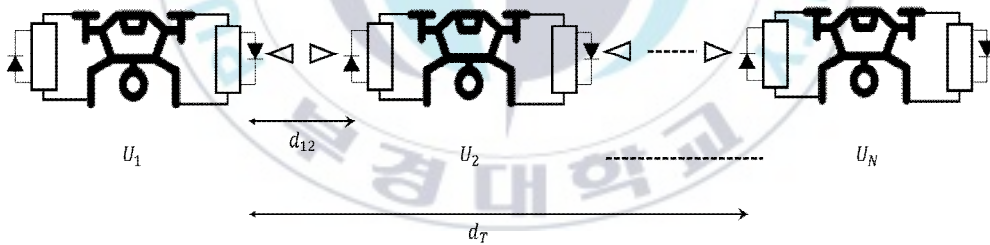


Figure 5.1. One-dimensional UAV optical ad-hoc network.

The proposed UAV ad-hoc network on one dimension is represented as shown in Figure 5.1. $d_{i,i+1}$, $i \in \{1, 2, \dots, N_u - 1\}$ is the distance between the i th and $(i+1)$ th UAV. Total number of UAVs are $N = N_u$. $d_{i,i+1}$ is a random variable that obeys Poisson point distribution. Let $d_T = \sum_{i=1}^{N_u-1} d_{i,i+1}$ be the total distance between the transmitter and the receiver. In a homogeneous

one-dimensional Poisson point process with rate (density) given by $r_u = N_u/d_T$, the probability of finding $n, n \leq N_u$, UAVs in a bounded borel $A \subset \mathbb{R}^S$, where A represents the one-dimensional space, can be express as

$$P_r [n \text{ UAVs in } A] = \exp(-u_d T(A)) \frac{(u_d T(A))^n}{n!} \quad (5.1)$$

where $T(A)$ represents the standard Lebesgue measure of A . u_d denotes the density of the UAVs in the given one-dimensional ad-hoc network. For the given network $r_u = u_d$. For the given one-dimensional system, $S = 1$.

In this section we derive the probability of connectivity for the one-dimensional ad-hoc network. In a Poisson point process, with $S=1$ and intensity (rate/density) r_u , the distance $d_{i,j}, j \neq i$ between the i th UAV and the j th UAV is distributed according to the generalized Gamma distribution as shown below

$$f_{d_{i,j}}(d_{i,j}) = \exp(-r_u K d_{i,j}) \frac{(r_u K d_{i,j})^{(j-i)}}{d_{i,j} \Gamma(j-i)} \quad (5.2)$$

where $K d_{i,j}$ denotes the volume of the one-dimensional ball of radius $d_{i,j}$. The coefficient K for one-dimensional network is equal to 2.

We describe that the given network is connected if all the neighboring nodes are connected. That is, UAV U_i is connected to U_{i-1} and U_{i+1} . This implies, the whole network is connected. The signal can effectively propagate from the transmitter to the receiver. Mathematically, the two neighboring UAVs i th and $(i+1)$ th are said to be connected if $d_{i,i+1} < d_{Th}$, where d_{Th} represents the transmitting range (threshold distance). If $d_{i,i+1} \geq d_{Th}$, the network becomes unconnected.

Mathematically, we define the probability of connectivity as

$$P_C = P_r(d_{i,j} < d_{Th}) = \int_0^{d_{Th}} f_{d_{i,j}}(d_{i,j}) d_{i,j} \quad (5.3)$$

Substituting (5.2) into (5.3), we obtained

$$P_C = \int_0^{d_{Th}} \exp(-r_u K d_{i,j}) \frac{(r_u K d_{i,j})^{(j-i)}}{d_{i,j} \Gamma(j-i)} d_{i,j} \quad (5.4)$$

$$\begin{aligned} &= \frac{2^n r_u^n}{\Gamma(n)} d_{i,j}^{n-1} \int \exp(-2r_u d_{i,j}) d_{i,j} \quad (5.5) \\ &= \frac{2^n r_u^n (n-1)}{\Gamma(n)} \int \frac{d_{i,j}^{(n-2)} \exp(-2r_u d_{i,j})}{(-2r_u)} d_{i,j} \end{aligned}$$

5.3 Results and Discussion

In this section, we analyze the link connectivity problem. The probability of connectivity relative to the UAV density is illustrated in Figure 5.2. The curves are obtained for different values of the transmission range. An important observation can be made that the performance gap between the different transmission range decreases as the transmission range increases.

The probability of connectivity among different neighbors is depicted in Figure 5.3. The curves are plotted for different UAV densities. The transmission range d_{Th} is set to 150 m. As expected, it is shown that as the order of the neighbor increases, the connectivity decreases significantly.

The probability of connectivity against the neighboring UAVs is illustrated in Figure 5.4. The end-to-end distance d_T between the transmitter and the receiver is set to 1 km. The transmission range (threshold distance) d_{Th} is set to 150 m. The UAV density r_u is set to 7 km^{-1} . As can be seen, as the neighboring UAV order is increases

to seventh, the connectivity drops to zero.

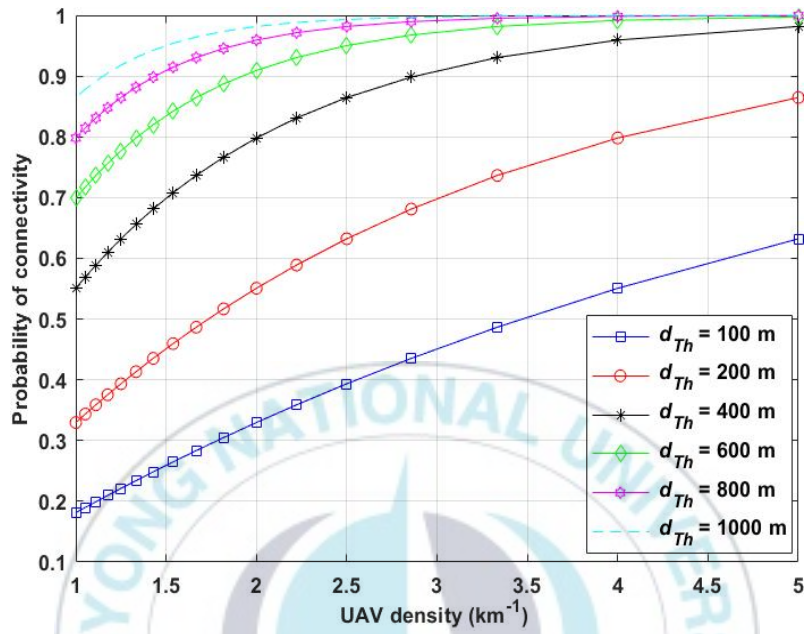


Figure. 5.2. Impact of the threshold distance on the probability of connectivity.

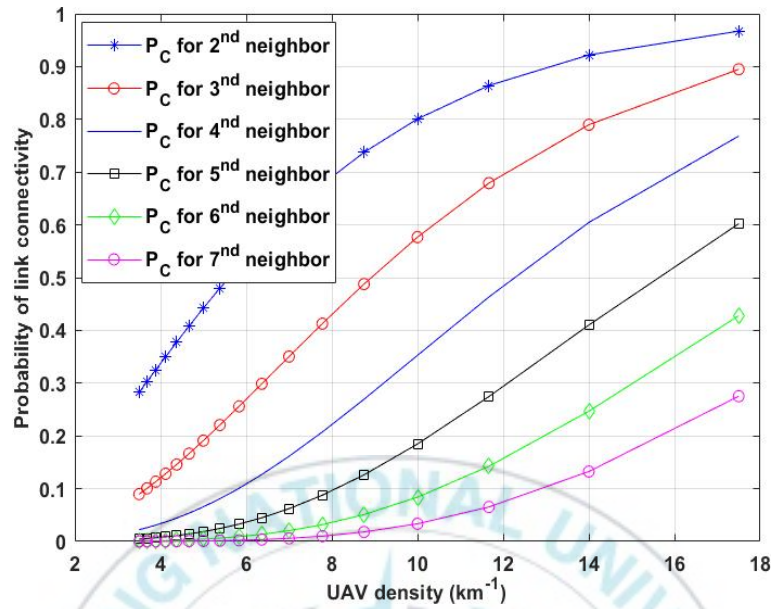


Figure. 5.3. Probability of connectivity relative to the UAV density for different neighbors.

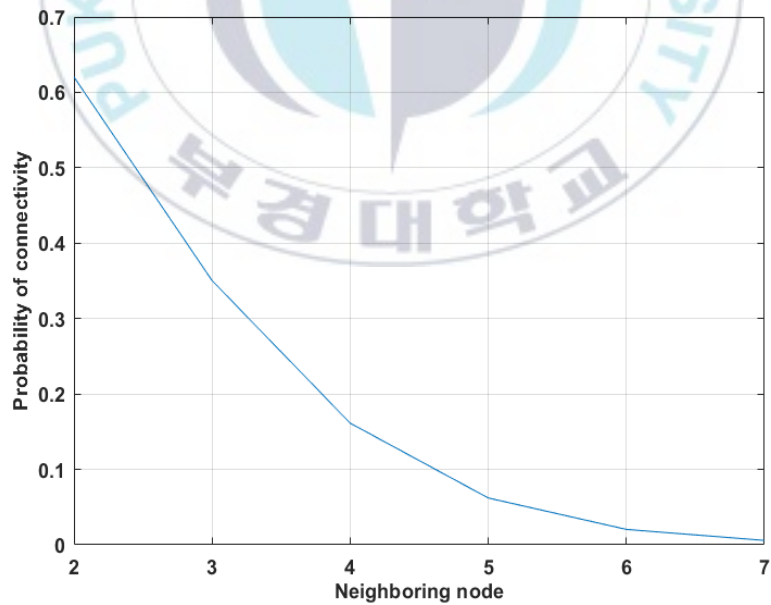


Figure 5.4. Probability of connectivity against the neighboring UAVs.

6. Energy Harvesting Scheme for Simultaneous Lightwave Information and Power Transfer

Underwater wireless communication using optical bands is also attracting attention. Communication using AUV underwater also has a number of challenge to overcome, one of which is power supply. In the deep sea, there is no way to get power, so you need a way to keep the AUV running. This problem can be solved by using SLIPT technologe when communicating using optical underwater [7][23].

6.1 Underwater Optical Wireless Communication

Recently, the demand for high-speed underwater wireless communication technology is increasing for use in environmental monitoring, resource exploration, warfare, etc. Currently, acoustic transmission is used for communication mainly used underwater. Acoustic transmission enables long-distance communication under water, but has a problem of severe inter-symbol interference due to low throughput Doppler effect, so it is not suitable for high-speed communication [25]. RF is also a candidate for underwater use. RF is capable of high data throughput over short distances(up to 10 m) and suffer from the mild Doppler effect. Underwater optical wireless communication is considered more suitable for underwater high-speed communication because it enables a higher data rate and a communication distance of 10 to 100 m compared to RF. However, since UOWC has several obstacles such as absorption, scattering, turbidity, and organic matter, more research is needed [4].

6.2 Simultaneous Lightwave Information and Power Transfer

For long-distance communication through UOWC, a repeater is needed to compensate for the relatively short communication distance. One of the methods is to use AUV as a repeater. However, power issues still remain even when AUVs are used as repeaters. There is a RF technology that can solve this problem, simultaneous wireless information and power transfer (SWIPT) technology. SWIPT has two processes: energy harvesting (EH) and information decoding (ID). EH is a process of charging through wireless channel, and ID is a process of receiving transmitted information [24]. RF can be replaced by visible light, it is termed as simultaneous lightwave information and power transfer (SLIPT). The time switching method is considered among several SLIPT schemes. When this scheme is employed, the receiver switches in time between the energy harvester and information decoder [7]. The received signal is split in the time domain for fractions of time α and $1 - \alpha$.

6.3 Optimal Energy Harvesting

In this section, we derive analytical expressions for the optimum value of α . Figure 6.1 illustrates the schematic diagram of the proposed time-splitting based SLIPT for underwater optical communications impaired by independent and non-identically distributed multi-layer turbulence-induced fading. Furthermore, it is assumed that channel fading remains constant during one time slot and changes independently between consecutive time slots.

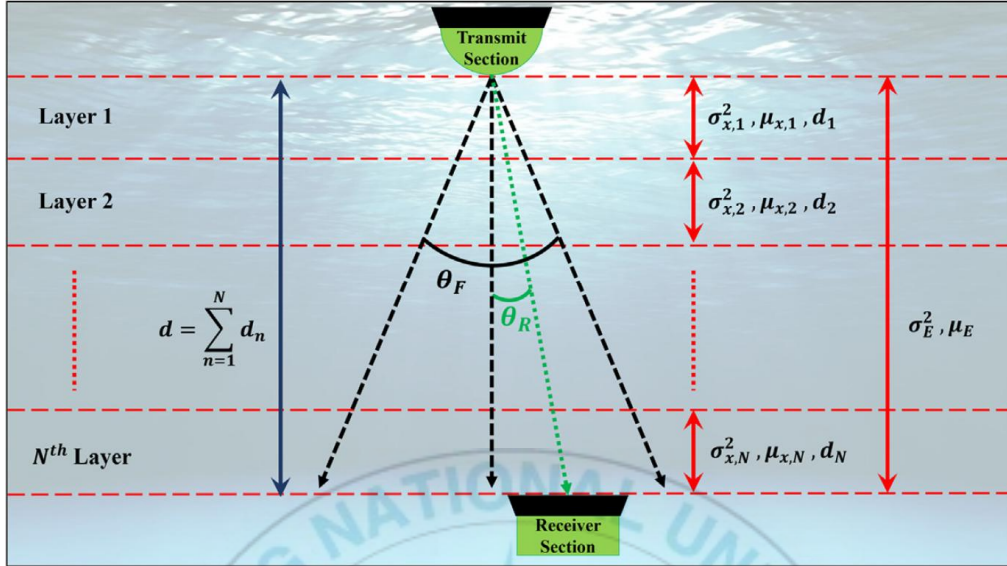


Figure 6.1. A schematic diagram showing the simultaneous information and power transfer.

In figure 6.1, θ_R is the angle between the transmitter axis and the received beam. θ_F is the full width transmitter beam divergence angle. d , σ_x^2 , σ_E^2 , μ_x , and μ_E respectively represent distance, variance of the turbulence-induced fading across the individual layer, overall variance corresponding to all layers, the mean of the fading coefficient across the individual layer, and the overall mean of the turbulence-induced fading coefficient.

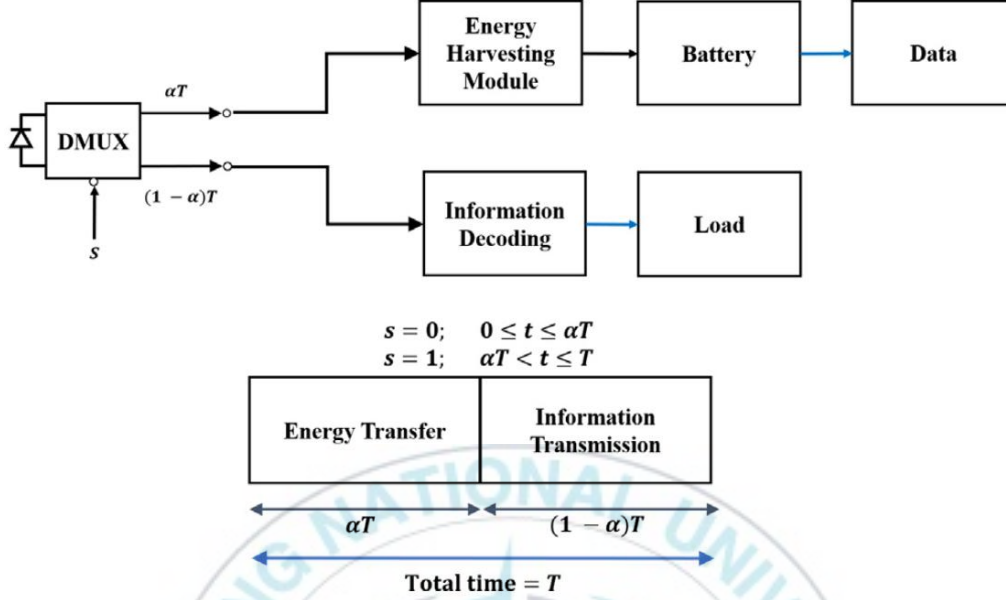


Figure 6.2 Receiver section.

In figure 6.2, αT represents the time allocated to energy harvesting. C_R represents the optical channel ratio and is defined as the ratio of the channel gain to the noise power. Their ratio can be expressed as

$$C_R = \frac{(E[I_E])^2 P_L}{\sigma_n^2} \quad (6.1)$$

where σ_n^2 represents the noise power, $E[\cdot]$ is expectation value, and P_L denotes the pathloss.

We consider a generalized scenario where for any arbitrary value of θ_R , the proposed analysis holds true. Following this, P_L can be modeled as

$$P_L = \eta_T \eta_R \exp \left[c(\lambda) \frac{d}{\cos(\theta_R)} \right] \left(\frac{D}{4d} \right)^2 \frac{\cos(\theta_R)}{\sin^2 \left(\frac{\theta_F}{4} \right)}, \quad \begin{aligned} \theta_F &\in (0, \theta_B], \theta_B < \pi \\ \theta_R &\in \left[0, \frac{\pi}{2} \right) \end{aligned}$$

(6.2)

where η_T and η_R denote the optical efficiency of the transmitter and the receiver, respectively. $c(\lambda)$ represents the total extinction coefficient and is related to the absorption coefficient $c_a(\lambda)$ and the scattering coefficient $c_s(\lambda)$ by $c(\lambda) = c_a(\lambda) + c_s(\lambda)$. It is important to note that, the absorption and the scattering coefficients are the functions of the transmitting wavelength. θ_F is the full-width transmitter beam divergence angle. D is the diameter of the receiver.

The received electrical signal can be modeled as

$$i(t) = SI_E P_L P_T(t) + w(t), \quad (6.3)$$

where S denotes the responsivity of the solar panel, I_E is the oceanic turbulence-induced fading, and $w(t)$ is the additive noise. P_T is the optical signal power emitted from the laser diode and can be modeled as

$$P_T(t) = P_{LD}[B + x(t)], \quad (6.4)$$

where P_{LD} is the optical transmit power and $x(t)$ corresponds to the voltage level of the transmitted information bit (bipolar OOK modulation) and can be expressed as

$$x(t) = \begin{cases} A \text{ volt} & \text{if bit 1 was transmitted} \\ -A \text{ volt} & \text{if bit 0 was transmitted} \end{cases} \quad (6.5)$$

where B in (6.4) represents the DC bias voltage and A in (6.5) denotes the peak amplitude. The energy harvesting, E , can be expressed as [17]

$$E = C_{FF} \left(\frac{1 - BER_{MAX}}{BER_{AVG}} \right) r h P_{LD} B V_t, \quad (6.6)$$

$$\times \left[\frac{2}{3} \phi(2\mu_x) + \frac{1}{6} \phi(2\mu_x + \sqrt{3}(2\sigma_x)) + \frac{1}{6} \phi(2\mu_x - \sqrt{3}(2\sigma_x)) \right]$$

where C_{FF} is the fill factor of solar panel, BER_{MAX} is the maximum of bit error rate, BER_{AVR} is the average of bit error rate, h is the attenuation term, r is the responsivity of the receiver, V_T is the thermal voltage, and $\phi(z)$ can be expressed as

$$\phi(z) = \exp(z) \ln(1 + r \exp(z) h P_{LD} B / I_o), \quad (6.7)$$

where I_o is the dark saturation current of solar panel [26].

6.3.1. Multi-layer turbulence channel

We consider an underwater communication link where the transmitter and the receiver are vertically deployed. Due to the vertically inhomogeneous nature of the underwater environment, the ocean or the seawater is generally vertically divided into multiple layers with different parameters that reflect real and practical environments. In vertical underwater communication links, the gradient of the salinity and the temperature change with the depth, thereby making the propagation properties of the communication link vary vertically [27]. Moreover, the extensive measurements conducted in the Pacific Ocean reveal that the strong temperature and salinity gradient prevail in most of the cases [28].

As the distance d between the transmitter and receiver changes over a vertical link, the gradient of the temperature and salinity will change. Therefore, it is convenient to model the realistic underwater vertical channel as a medium with multiple layers. We consider a multi-layer

turbulence channel with N layers. For the case of weak oceanic turbulence, the fading of the optical signal due to the oceanic turbulence follows a log-normal distribution. For the n th layer, it can be modeled as

$$f_{I_n}(I_n) = \frac{1}{I_n \sqrt{2\pi(4\sigma_{x,n}^2)}} \exp\left(-\frac{(\ln(I_n) - 2\mu_{x,n})^2}{2(4\sigma_{x,n}^2)}\right), \quad (6.8)$$

where $\mu_{x,n} = E[X_n = 0.5\ln(I_n)]$ represents the mean of the logamplitude coefficient X_n , $\sigma_{x,n}^2 = \frac{\sum_{i=1}^L (X_i - \bar{X})^2}{L-1}$ is the variance of the log-amplitude coefficient X_n , and L is the number of observations, that is, the number of samples. The parameters correspond to the turbulence effect on the n th layer with thickness d_n being $\{\sigma_{x,n}^2, \mu_{x,n}\}$. It is to be noted that, if d_n is small, it is safe to assume that within any n th layer, the turbulence parameters $\sigma_{x,n}^2$ and $\mu_{x,n}$ are constant. Therefore, the fading coefficients $\{\sigma_{x,n}^2, \mu_{x,n}\} \forall n \in \{1, \dots, N\}$ can be thought of independent and non-identically distributed. Following this, the effective fading coefficient I_E over the N number of layers can readily be written as

$$I_E = \prod_{n=1}^N I_n = I_1 \times I_2 \times \dots \times I_N, \quad (6.9)$$

with the PDF of the effective distribution written as

$$f_{I_E}(I_E) = \frac{1}{I_E \sqrt{2\pi(4\sigma_E^2)}} \exp\left(-\frac{(\ln(I_E) - 2\mu_E)^2}{2(4\sigma_E^2)}\right), \quad (6.10)$$

where the effective coefficients σ_E^2 and μ_E are given by [29]

$$\sigma_E^2 = \sum_{n=1}^N 4\sigma_{x,n}^2, \quad (6.11)$$

and

$$\mu_E = \sum_{n=1}^N 2\mu_{x,n} \quad (6.12)$$

6.4. Problem Formulation

In this section, we focus on the optimization of the time-splitting ratio. This work adopts a utility maximization framework in which each energy harvesting rate has an associated utility function. We model the utility function as a concave function of the achievable data rate. The problem statement can then be formulated as: Find the optimum value of the time splitting ratio α for maximum data rate (throughput) and maximum energy harvesting for the underwater optical channel impaired by independent and non-identically distributed multi-layer turbulence fading. Mathematically, it can be stated as

$$\max_{\alpha \in [0,1]} R(X) \quad \text{subject to } X > 0 \quad (6.13)$$

where R represents the data rate and X denotes the energy harvesting rate given by $X = \frac{E}{T_{EH}}$.

6.4.1. Optimization problem with deterministic energy harvesting rate

Because there is no transmit power constraint, the data rate as a function of the channel parameters and α can be written as [30]

$$R = (1 - \alpha T) \log_2 \left(C_R \times \frac{X\alpha T}{(1 - \alpha T)} \right). \quad (6.14)$$

It is evident from (6.14) that the data rate R is a concave function of α . Therefore, finding an optimal value of α is an example of concave optimization. Differentiating (6.14) with respect to α yields

$$\frac{d}{d\alpha} R = -T \log_2 \left(C_R \times \frac{X\alpha T}{(1 - \alpha T)} \right) + \frac{1}{\alpha \times \log_e 2}, \quad (6.15)$$

Solving for the second derivative of R with respect to α yields

$$\frac{d^2}{d\alpha^2} R = -\frac{1}{(\log_e 2) \alpha^2 (1 - \alpha T)}, \quad (6.16)$$

Since we know that α can attain a value such that $0 \leq \alpha \leq 1$, for a unit time, (16) will always result in a negative value, that is,

$$\frac{d^2}{d\alpha^2} R < 0, \quad \forall \alpha, C_R. \quad (6.17)$$

Analytically, (17) verifies our claim that the throughput and the energy harvesting maximization problem with respect to the parameter α is a concave optimization problem.

Now that R is a concave function, in order to find the optimal value of α , we need to equate $\frac{d}{d\alpha} R = 0$. It yields

$$\alpha \log_2 \left(C_R \times \frac{X\alpha T}{(1-\alpha T)} \right) = \frac{1}{T \times \log_e 2}, \quad (6.18)$$

It is important to note that (6.18) cannot be solved directly. Eq. (6.18) can be solved by using the identity

$$W(x) = xe^{-w(x)}, \quad (6.19)$$

where $W(\cdot)$ represent the Lambert W function [31].

$$\frac{1}{\alpha} = T - W \left(-\frac{1}{T} \exp(1 - \log_e C_R - \log_e XT) \right) T \quad (6.20)$$

Therefore, the optimum value of α is derived analytically as,

$$\alpha = \frac{1}{\left[T \left(1 - W \left(-\frac{1}{T} \exp(1 - \log_e C_R - \log_e XT) \right) \right) \right]}. \quad (6.21)$$

6.4.2. Optimization problem with nondeterministic energy harvesting rate

Considering the optimization problem with stochastic energy harvesting rate, the optimization problem can be stated as

$$\max_{\alpha \in [0,1]} E[R(X)] \quad \text{subject to } X > 0, \quad (6.22)$$

where $E[R(X)]$ is the long-term average of the data rate. Since the energy harvesting rate X is a random variable, the appropriate distribution to model X accurately is the Gamma distribution [32]. Following this, X can be modeled as $X \sim \Gamma(g_1, g_2)$, where g_1 and g_2

represent the shape parameters such that $g_1, g_2 > 0$. The PDF of X can then be modeled as

$$f_x(X) = \frac{x^{g_1-1}}{g_2^{g_1} \Gamma(g_1)} \exp\left(-\frac{x}{g_2}\right). \quad (6.23)$$

Utilizing the maximization problem illustrated in (6.22), we obtain

$$\max_{\alpha \in [0,1]} R(X) = (1-\alpha T) E\left[\log_2\left(C_R \times \frac{X\alpha T}{(1-\alpha T)}\right)\right]. \quad (24)$$

Following (6.23) and (6.24), the distribution of the random variable $Z \equiv C_R \times \frac{X\alpha T}{(1-\alpha T)}$ can readily be obtained as

$$f_Z(Z) = \frac{Z^{g_1-1}}{\Gamma(g_1)} \left(\frac{1-\alpha T}{\alpha T C_R g_2}\right)^{g_1} \exp\left(-\frac{Z(1-\alpha T)}{\alpha T C_R g_2}\right). \quad (6.25)$$

With high C_R condition and following (6.22), (6.23), and (6.4), the longterm expected value of $R(X)$ can be derived as [33]

$$E[R(X)] = \frac{1-\alpha T}{\ln 2} \left[\frac{d}{dg_1} \left(\int_0^\infty t^{g_1-1} \exp(-t) dt \right) + \ln\left(\frac{\alpha T C_R g_2}{1-\alpha T}\right) \right]. \quad (6.26)$$

Differentiating (6.26) with respect to α yields

$$\begin{aligned} \frac{d}{d\alpha} E[R(X)] &= \left[\frac{TC_R g_2}{(1-\alpha T)^2 \ln 2} \right] \times \left[\frac{1-\alpha T}{\alpha T C_R g_2} - T \ln\left(\frac{\alpha T C_R g_2}{1-\alpha T}\right) \right] \\ &- \frac{T}{\ln 2} \left[\frac{d}{dg_1} \left(\int_0^\infty t^{g_1-1} \exp(-t) dt \right) \right] \end{aligned} \quad (6.27)$$

It can be readily shown that $\frac{d^2 E[R(X)]}{d(\alpha T)^2} < 0$, for $0 < \alpha T < 1$. Therefore the optimization problem is concave and has a unique solution given by

$$\alpha T = \frac{1}{W\left(C_R g_2 \exp\left[\frac{d}{dg_1}\left(\int_0^\infty t^{g_1-1} \exp(-t) dt\right) - 1\right]\right) + 1}, \quad (6.28)$$

where $W(\cdot)$ is the Lambert W function defined in (6.19).

6.5 Results and Discussion



Table 6.1 Simulation parameters for underwater optimal α value.

Parameter	Value
Fill factor of the solar panel, C_{FF}	0.75
BER_{MAX}	1×10^{-6}
BER_{AVG}	1×10^{-4}
Responsivity, r	40 %
P_{LD}	30 W/A
DC bias, B	2
Thermal voltage, V_t	25×10^{-3} V
Variance, $\sigma_{x,j}^2 \quad \forall j \in \{1, \dots, n\}$	1.04×10^{-3}
Mean, $\mu_{x,j} \quad \forall j \in \{1, \dots, n\}$	$-\sigma_{x,j}^2$
Wavelength	532 nm
Receiver aperture diameter, D_R	5×10^{-2} m
Full width transmitter beam divergence angle, θ_F	6°
Correction coefficients, ρ	0.13
Extinction coefficients, c (pure water)	0.056
Extinction coefficients, c (clear ocean water)	0.150
Extinction coefficients, c (coastal water)	0.305
Maximum input bias currents	45 mA
Minimum input bias currents	25 mA
Symbol duration, T	1×10^{-6} s

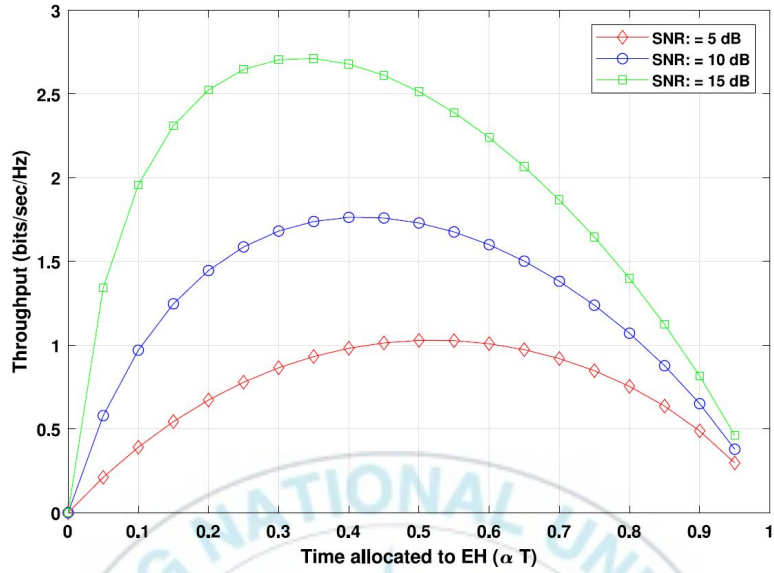


Figure 6.3. Throughput (bits/s/Hz) relative to the time allocated to the energy harvesting (αT).

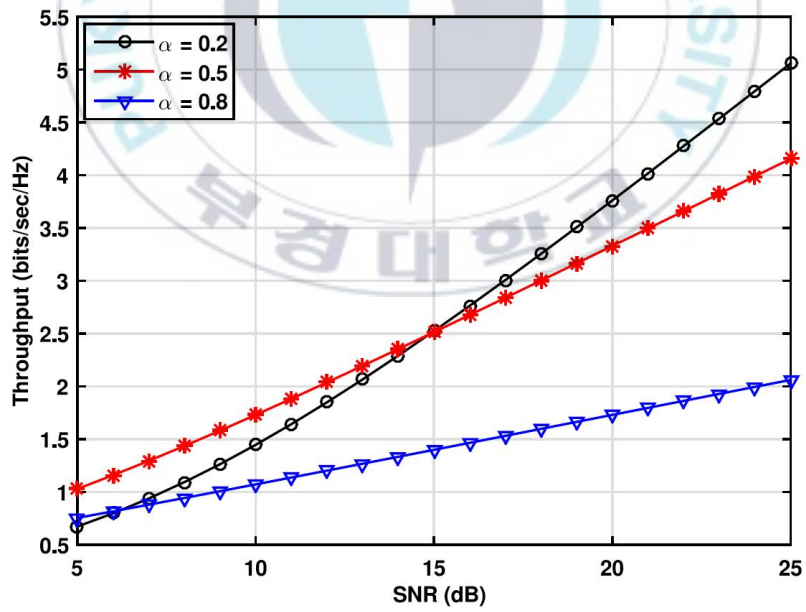


Figure 6.4. Throughput (bits/s/Hz) relative to the received SNR (dB).

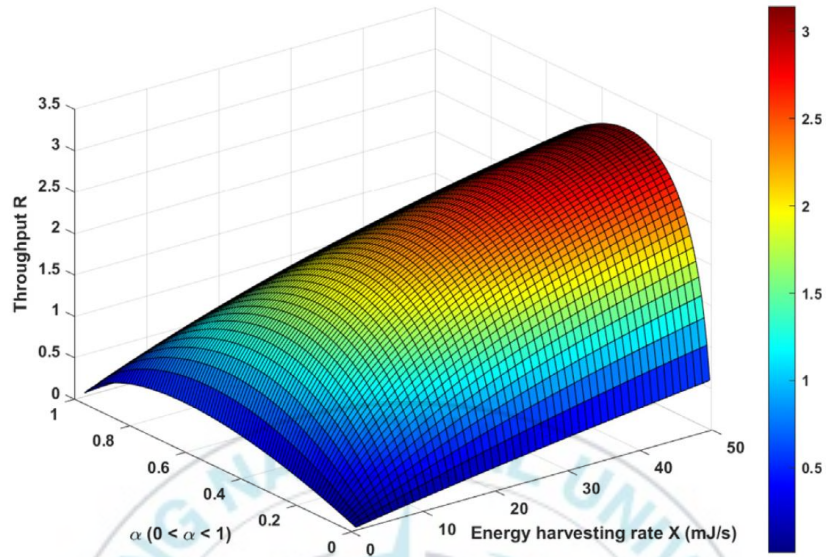


Figure 6.5. Throughput (bits/s/Hz) as a function of α and the energy harvesting rate X (mJ/s).

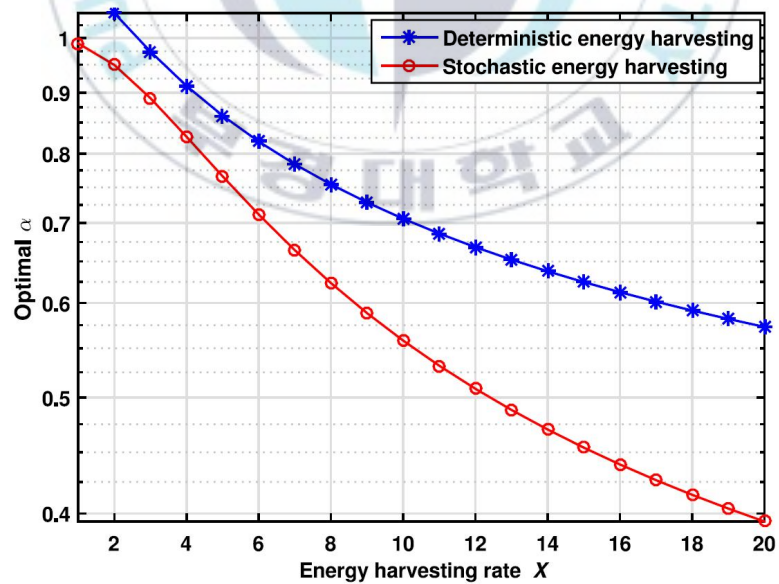


Figure 6.6. The optimum α relative to the energy harvesting rate X (mJ/s).

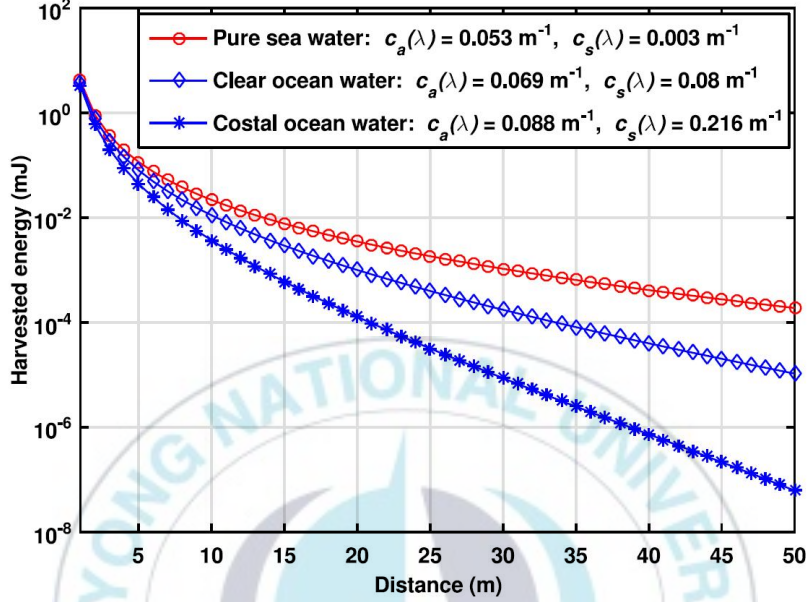


Figure 6.7. Energy harvesting relative to the distance between the transmitter and receiver.

To verify the optimum value of α , we conduct simulations with the parameters presented in Table 6.1. SNR represents the signal power to noise power ratio, i.e., $SNR = P_T \times C_R$.

Figure 6.3 illustrates the throughput relative to the fraction of time allocated for energy harvesting. In the time-splitting (time-switching) approach, the throughput is a concave function of α . The achievable throughput has only one global maximum, that is, it first increases when $\alpha < \alpha_{optimum}$, then attains its maximum value at $\alpha = \alpha_{optimum}$, and decreases when $\alpha > \alpha_{optimum}$, where $\alpha_{optimum}$ represents the optimum value of α . As the transmit power increases, the optimum value of α reduces. It is important to note that, the optimum value of α is always less than 0.5.

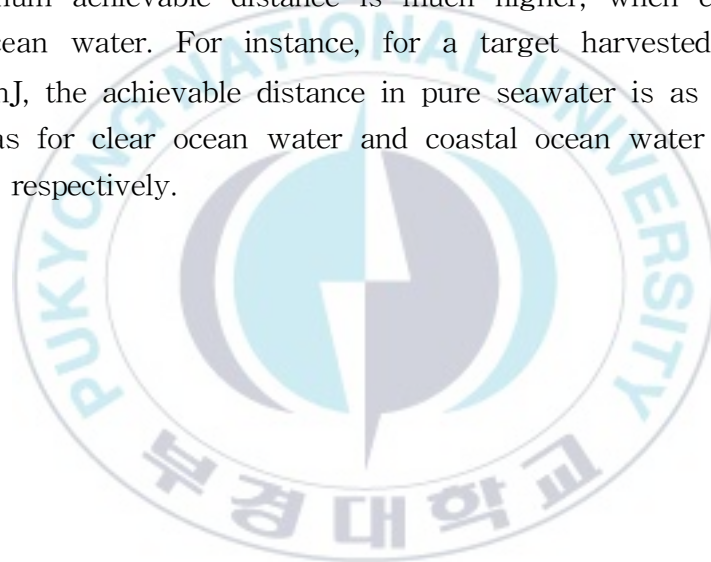
Figure 6.4 shows the throughput as a function of the received SNR

for different values of α . As inferred from the results, an important observation can be made that the optimum value of α depends upon the value of the received SNR and given channel conditions. For instance, at the received SNR of 5 dB, the curve at $\alpha = 0.8$ yields more throughput than $\alpha = 0.2$, whereas $\alpha = 0.5$ is the optimum value and results in the highest throughput. That is, $R|_{\alpha=0.5} > R|_{\alpha=0.8} > R|_{\alpha=0.2}$. Interestingly, contrary to the results obtained at low SNRs, when increasing the SNR to 15 dB, the curve at $\alpha = 0.2$ results in higher data rate when compared with the data rate obtained with $\alpha = 0.8$. That is, $R|_{\alpha=0.5} = R|_{\alpha=0.2} > R|_{\alpha=0.8}$. Moreover, on increasing the SNR further, the optimum value changes to $\alpha = 0.2$. Specifically, $R|_{\alpha=0.2} > R|_{\alpha=0.5} > R|_{\alpha=0.8}$.

The throughput as a function of α and the energy harvesting rate X are illustrated in Figure 6.5. With small α , the amount of energy harvested by the user is small. At the optimum value of α , the user harvests more energy, with throughput also increasing at $\alpha = \alpha_{optimum}$. However, as α becomes larger than $\alpha_{optimum}$, the throughput decreases due to the reduction in the time allocated to information transmission. Figure 6.6 shows the optimal value of α relative to the energy harvesting rate X for the deterministic and stochastic energy harvesting rates. Interestingly, it can be seen that as the energy harvesting rate X increases, the optimal choice of α tends to be allocating a smaller fraction of time for energy harvesting. This is because $1 - \alpha T$ dominates the optimization such that with high-performance energy harvesting, extending the time for data transmission is preferred. Another important observation that can be inferred from the results is that at a given value of SNR, the optimum value of α required in the stochastic case is slightly lower than the one required in the deterministic case.

The energy harvesting relative to the link range for different types of water is illustrated in Figure 6.7. Typical values of the absorption and

the scattering coefficients at the wavelength of 532 nm are also depicted [34]. It can be said that the coastal water condition yields severe performance degradation when compared to seawater and clear ocean water. This can be attributed to the fact that the coastal ocean water has a relatively higher concentration of planktonic matters, detritus, and mineral components that severely impact the absorption and the scattering phenomena inside the water and thus results in a minimum harvested energy. Moreover, due to less significant scattering in pure seawater case with the scattering coefficient $c_s(\lambda) = 0.003 m^{-1}$, the maximum achievable distance is much higher, when compared to coastal ocean water. For instance, for a target harvested energy of 3×10^{-4} mJ, the achievable distance in pure seawater is as large as 50 m, whereas for clear ocean water and coastal ocean water it is 29 m and 18 m, respectively.



7. Conclusion

This thesis has delivered the design and modeling of various unmanned vehicle communication link and has explored the link connectivity between the unmanned vehicle. This thesis has also explored the optimal parameter of time splitting of SLIPT for power problem in communication between AUVs.

In the first part of the thesis, we have proposed the design and implementation of the maximal selection transmit diversity scheme for the ground-to-UAV optical communication link impaired by the turbulence-induced fading. It has been found that the MSTD scheme always showed better results than the existing single branch scheme regardless of the turbulence intensity.

In the next study, we have proposed a transmission technique for ground-to-UAV link over correlated optical channel. In particular, we have proposed dual branch SSC with frequency-shift keying sub-carrier intensity modulation. The turbulence-induced fading follows the gamma-gamma distribution. The closed-form expressions for the PDF of the instantaneous received SNR and the average BER are derived. In addition, we analyze the impact of channel correlation.

The next part of the thesis is focused on the propagation characteristics of the Laguerre-Gaussian beam over a UAV-to-ground based optical communication link. The loss due to the hovering UAV is also analyzed.

The next study have considered one-dimensional UAV ad-hoc optical network such that the randomly distributed UAVs obeys the Poisson point process. We have derived the probability of connectivity as a function of the UAV density and the transmission range. Subsequently, we have characterized the influence of the various system parameters.

The last section have considered an optimization problem in the

SLIPT scheme. The optimal charging time in the time-switching method of the SLIPT scheme has been found to compensate for the power-poor underwater AUV network. We have proved the concavity of the achievable throughput and proposed the optimal value of the fraction of time allocated exclusively to energy harvesting as a function of energy harvesting rate. In addition, we have numerically analyzed how the optimal value and the maximal achievable throughput vary with the energy harvesting rate and further validated its optimality via simulation results.

Through the first three parts, it has been possible to find ways to improve communication performance in the form of a new communication network using unmanned vehicles. The fourth part contributed to the more stable unmanned vehicle communication environment by studying connectivity between unmanned vehicles. The last part contributed to solving the power shortage problem that can occur when communicating using an unmanned vehicle underwater.

References

- [1] S. Mumtaz et al., "Terahertz communication for vehicular networks", *IEEE Trans. Veh. Technol.*, vol. 66, pp. 5617–5625, Jul. 2017.
- [2] M. A. Khalighi and M. Uysal, "Survey on Free Space Optical Communication: A Communication Theory Perspective," in *IEEE Communications Surveys & Tutorials*, vol. 16, no. 4, pp. 2231–2258, Fourthquarter 2014.
- [3] H. Kaushal and G. Kaddoum, "Optical Communication in Space: Challenges and Mitigation Techniques," in *IEEE Communications Surveys & Tutorials*, vol. 19, no. 1, pp. 57–96, Firstquarter 2017.
- [4] H. Kaushal and G. Kaddoum, "Underwater Optical Wireless Communication," in *IEEE Access*, vol. 4, pp. 1518–1547, 2016.
- [5] Valavanis, Kimon P., and George J. Vachtsevanos, eds. *Handbook of unmanned aerial vehicles*. Vol. 1. Dordrecht: Springer Netherlands, 2015.
- [6] W. Fawaz, C. Abou-Rjeily and C. Assi, "UAV-Aided Cooperation for FSO Communication Systems," in *IEEE Communications Magazine*, vol. 56, no. 1, pp. 70–75, Jan. 2018.
- [7] S. Ghasvarianjahromi, M. Karbalayghareh, P. D. Diamantoulakis, G. K. Karagiannidis and M. Uysal, "Simultaneous Lightwave Information and Power Transfer in Underwater Visible Light Communications," 2019 *IEEE 30th Annual International Symposium on Personal, Indoor and Mobile Radio Communications (PIMRC)*, 2019, pp. 1–6.
- [8] M. Z. Chowdhury, M. Shahjalal, S. Ahmed and Y. M. Jang, "6G

Wireless Communication Systems: Applications, Requirements, Technologies, Challenges, and Research Directions," in IEEE Open Journal of the Communications Society, vol. 1, pp. 957-975, 2020.

[9] Z. Ghassemlooy, S. Arnon, M. Uysal, Z. Xu and J. Cheng, "Emerging Optical Wireless Communications-Advances and Challenges," in IEEE Journal on Selected Areas in Communications, vol. 33, no. 9, pp. 1738-1749, Sept. 2015.

[10] M. T. Dabiri et al., "UAV-Assisted Free Space Optical Communication System With Amplify-and-Forward Relaying," in IEEE Transactions on Vehicular Technology, vol. 70, no. 9, pp. 8926-8936, Sept. 2021.

[11] 여찬일, et al. "UAV 기반 FSO 무선통신 네트워크 기술 동향." [ETRI] 전자통신동향분석 35.2 (2020): 38-49.

[12] Y. Dong, M. Z. Hassan, J. Cheng, M. J. Hossain and V. C. M. Leung, "An Edge Computing Empowered Radio Access Network with UAV-Mounted FSO Fronthaul and Backhaul: Key Challenges and Approaches," in IEEE Wireless Communications, vol. 25, no. 3, pp. 154-160, JUNE 2018.

[13] Sudhanshu Arya and Yeon Ho Chung, "Amplify-and-forward multihop non-line-of-sight ultraviolet communication in the gamma-gamma fading channel," J. Opt. Commun. Netw. 11, 422-436 (2019)

[14] S. Arya and Y. H. Chung, "Spectrum Sensing for Optical Wireless Scattering Communications Over Málaga Fading-A Cooperative Approach With Hard Decision Fusion," in IEEE Transactions on Communications, vol. 69, no. 7, pp. 4615-4631, July 2021.

- [15] Arya, Sudhanshu, and Yeon Ho Chung. "Maximal Selective Transmit Diversity for Petahertz Wireless Communications With Continuous Waveform Detector." *IEEE Access* 9 (2021): 118005-118018.
- [16] M. T. Dabiri, H. Savojbolaghchi, and S. M. Sajad Sadough, "On the ergodic capacity of ground-to-uav free-space optical communications," in 2019 2nd West Asian Colloquium on Optical Wireless Communications (WACOWC), 2019, pp. 176 - 179.
- [17] V. S. Adamchik and O. I. Marichev. 1990. The algorithm for calculating integrals of hypergeometric type functions and its realization in REDUCE system. In Proceedings of the international symposium on Symbolic and algebraic computation (ISSAC '90). Association for Computing Machinery, New York, NY, USA, 212 - 224.
- [18] I. S. Gradshteyn and I. M. Ryzhik, Table of integrals, series, and products, 7th ed. Elsevier/Academic Press, Amsterdam, 2007.
- [19] S. Arya and Y. H. Chung, "Maximal selective transmit diversity for petahertz wireless communications with continuous waveform detector," *IEEE Access*, vol. 9, pp. 118 005 - 118 018, 2021.
- [20] S. Arya and Y. H. Chung, "M-PSK Subcarrier Intensity Modulation with Switch-and-Stay Diversity for NLOS Ultraviolet Communication," *TENCON 2018 - 2018 IEEE Region 10 Conference*, 2018, pp. 0524-0529.
- [21] Prudnikov, A.P., Brychkov, I.A. and Marichev, O.I, Integrals and Series: More special functions, Gordon and Breach Science Publishers, vol. 3, (1986).

- [22] S. Arya and Y. H. Chung, "High-Performance and High-Capacity Ultraviolet Communication With Orbital Angular Momentum," in *IEEE Access*, vol. 7, pp. 116734-116740, 2019.
- [23] C. Gussen, P. Diniz, M. Campos, W. Martins, F. Costa, J. Gois, A survey of underwater wireless communication technologies, *Journal of Communication and Information Systems* 31 (1).
- [24] T. D. Ponnimbaduge Perera, D. N. K. Jayakody, S. K. Sharma, S. Chatzinotas, J. Li, Simultaneous wireless information and power transfer (swipt): Recent advances and future challenges, *IEEE Communications Surveys Tutorials* 20 (1) (2018) 264 - 302.
- [25] S. Basagni, M. Conti, S. Giordano, I. Stojmenovic, *Advances in Underwater Acoustic Networking*, 2013, pp. 804 - 852.
- [26] S. Ghasvarianjahromi, M. Karbalayghareh, P. D. Diamantoulakis, G. K. Karagiannidis, M. Uysal, Simultaneous lightwave information and power transfer in underwater visible light communications, in: *2019 IEEE 30th Annual International Symposium on Personal, Indoor and Mobile Radio Communications (PIMRC)*, 2019, pp. 1 - 6.
- [27] M. Elamassie, M. Uysal, Vertical underwater visible light communication links: channel modeling and performance analysis, *IEEE Trans. Wireless Commun.* 19 (10) (2020) 6948 - 6959.
- [28] V. Nikishov, V. Nikishov, Spectrum of turbulent fluctuations of the sea-water refraction index, *Int. J. Fluid Mech. Res.* 27 (1) (2000).
- [29] M. Elamassie, M. Uysal, Performance characterization of vertical

underwater VLC links in the presence of turbulence, in: 2018 11th International Symposium on Communication Systems, Networks Digital Signal Processing (CSNDSP), 2018, pp. 1 - 6.

[30] P.D. Diamantoulakis, G.K. Karagiannidis, Z. Ding, Simultaneous lightwave information and power transfer (SLIPT), *IEEE Trans. Green Commun. Netw.* 2 (3) (2018) 764 - 773.

[31] R.M. Corless, G.H. Gonnet, D.E. Hare, D.J. Jeffrey, D.E. Knuth, On the LambertW function, *Adv. Comput. Math.* 5 (1) (1996) 329 - 359.

[32] S. Luo, R. Zhang, T.J. Lim, Optimal save-then-transmit protocol for energy harvesting wireless transmitters, *IEEE Trans. Wireless Commun.* 12 (3) (2013) 1196 - 1207.

[33] S. Yin, E. Zhang, J. Li, L. Yin, S. Li, Throughput optimization for selfpowered wireless communications with variable energy harvesting rate, in 2013 IEEE Wireless Communications and Networking Conference (WCNC), 2013, pp. 830 - 835.

[34] G. Schirripa Spagnolo, L. Cozzella, F. Leccese, Underwater optical wireless communications: Overview, *Sensors* 20 (8) (2020) 2261.

List of Publications

Journal Papers

- [1] **Yeong Hae Kim**, Sudhanshu Arya, and Yeon Ho Chung. (2021). *An optimal energy harvesting scheme for simultaneous lightwave information and power transfer over multi-layer turbulence-induced underwater channel*. Optics Communications 501: 127382.



Conference Papers

- [1] **Yeong Hae Kim**, Sudhanshu Arya, Prakriti Saxena, and Yeon Ho Chung. (2021). *Impact of Hovering on Laguerre-Gaussian Beam Propagation for UAV-to-Ground Optical Communications*. 2021 International Conference on Information and Communication Technology Convergence (ICTC), IEEE.
- [2] **Yeong Hae Kim**, Chan Woong Park, Sudhanshu Arya, and Yeon Ho Chung. (2022). *An Experimental Study of Visible Light based UAV-to-ground Links*. 한국통신학회 학술대회논문집, 369-371. (우수논문상)
- [3] Sudhanshu Arya, **Yeong Hae Kim**, and Yeon Ho Chung. (2022). *Non-cooperative Game Theoretic Approach to Capacity Maximization in Multiuser Optical Scattering Communications*. 한국통신학회 학술대회논문집, p.433-435.
- [4] **Yeong Hae Kim**, Sudhanshu Arya, and Yeon Ho Chung. (2022). *Novel FSK-SIM Scheme with Switch-and-Stay Combining for Ground-to-UAV Optical Links over Realistic Correlated Channels*. 한국통신학회 학술대회논문집, p.431-432.
- [5] **Yeong Hae Kim**, Sudhanshu Arya, and Yeon Ho Chung. (2021). *Optical Array Selection Transmit Diversity Scheme for Ground-to-UAV Optical Links*. 한국통신학회 학술대회논문집, p.227-230.
- [6] **Yeong Hae Kim**, Young Jae Moon, Sudhanshu Arya, and Yeon Ho Chung. (2022). *Indoor Visible Light LOS Channel Estimation using Support Vector Regression*. Proceedings of International Conference on Maritime IT Convergence (ICMIC), Jeju.

[7] **Yeong Hae Kim**, Sudhanshu Arya, and Yeon Ho Chung. (2021). *On the Link Connectivity in One-Dimensional UAV Optical Ad-Hoc Network*. 대한전자공학회 학술심포지움 논문집.

[8] **Yeong Hae Kim**, Jung Min Park, Sudhanshu Arya, and Yeon Ho Chung. (2020). *Analysis of Optimal Energy Harvesting Time for Time Splitting based SLIPT*. 대한전자공학회 학술심포지움 논문집.

[9] Jung Min Park, Sudhanshu Arya, **Yeong Hae Kim**, and Yeon Ho Chung. (2020). *Noise signal analysis based on artificial neural network*. 대한전자공학회 학술심포지움 논문집.

